



PRIMUS + DEEP2: CLUSTERING OF X-RAY, RADIO, AND IR-AGNs AT $z \sim 0.7$

ALEXANDER J. MENDEZ^{1,2}, ALISON L. COIL¹, JAMES AIRD³, RAMIN A. SKIBBA¹, ALEKSANDAR M. DIAMOND-STANIC⁴,
JOHN MOUSTAKAS⁵, MICHAEL R. BLANTON⁶, RICHARD J. COOL⁷, DANIEL J. EISENSTEIN⁸,
KENNETH C. WONG⁹, AND GUANGTUN ZHU²

¹ Center for Astrophysics and Space Sciences, Department of Physics, University of California, 9500 Gilman Drive,
La Jolla, San Diego, CA 92093, USA; ajmendez@jhu.edu

² Department of Physics and Astronomy, Johns Hopkins University, 3400 North Charles Street, Baltimore, MD 21218, USA

³ Department of Physics, Durham University, Durham DH1 3LE, UK

⁴ Department of Astronomy, University of Wisconsin-Madison, Madison, WI 53706-1582, USA

⁵ Department of Physics and Astronomy, Siena College, 515 Loudon Road, Loudonville, NY 12211, USA

⁶ Center for Cosmology and Particle Physics, Department of Physics, New York University, 4 Washington Place, New York, NY 10003, USA

⁷ MMT Observatory, 1540 East Second Street, University of Arizona, Tucson, AZ 85721, USA

⁸ Harvard College Observatory, 60 Garden Street, Cambridge, MA 02138, USA

⁹ Steward Observatory, The University of Arizona, 933 North Cherry Avenue, Tucson, AZ 85721, USA

Received 2015 April 23; accepted 2016 February 11; published 2016 April 11

ABSTRACT

We measure the clustering of X-ray, radio, and mid-IR-selected active galactic nuclei (AGNs) at $0.2 < z < 1.2$ using multi-wavelength imaging and spectroscopic redshifts from the PRIMUS and DEEP2 redshift surveys, covering seven separate fields spanning $\sim 10\text{deg}^2$. Using the cross-correlation of AGNs with dense galaxy samples, we measure the clustering scale length and slope, as well as the bias, of AGNs selected at different wavelengths. Similar to previous studies, we find that X-ray and radio AGNs are more clustered than mid-IR-selected AGNs. We further compare the clustering of each AGN sample with matched galaxy samples designed to have the same stellar mass, star-formation rate (SFR), and redshift distributions as the AGN host galaxies and find no significant differences between their clustering properties. The observed differences in the clustering of AGNs selected at different wavelengths can therefore be explained by the clustering differences of their host populations, which have different distributions in both stellar mass and SFR. Selection biases inherent in AGN selection therefore determine the clustering of observed AGN samples. We further find no significant difference between the clustering of obscured and unobscured AGNs, using IRAC or *Wide-field Infrared Survey Explorer* colors or X-ray hardness ratio.

Key words: galaxies: active – galaxies: evolution – infrared: galaxies – radio continuum: galaxies – X-rays: galaxies

1. INTRODUCTION

It is now well established that most galaxies host a supermassive black hole (SMBH; e.g., Kormendy & Richstone 1995; Richstone et al. 1998; Ferrarese & Ford 2005; Kormendy & Ho 2013). However, it is not well understood what physical processes trigger intense episodes of accretion onto the SMBH, creating an observed active galactic nucleus (AGN). The broad similarities between the cosmic star-formation history and AGN mass accretion history, both peaking at $z \sim 2$ and declining sharply at lower redshift (e.g., Soltan 1982; Madau et al. 1996; Franceschini et al. 1999; Ueda et al. 2003; Zheng et al. 2009; Serjeant et al. 2010; Aird et al. 2015), and the relatively tight observed correlation between SMBH mass and mass of the host galaxy bulge (M - σ relationship; e.g., Magorrian et al. 1998; Gebhardt et al. 2000; Tremaine et al. 2002) hint at the possibility of a coeval evolution between SMBHs and their host galaxies.

The vast scale difference between galaxies and SMBHs, coupled with the relative rarity of the active accretion phase, has made it difficult to determine the physical mechanism(s) connecting galaxy and AGN growth. Constraining the triggering and fueling mechanism(s) of AGNs is key to uncovering the relevant physics connecting SMBHs and their host galaxies.

Clustering measurements on scales larger than a typical dark matter halo ($r_p \gtrsim 1 h^{-1} \text{Mpc}$) estimate the mean dark matter halo mass of AGN hosts, effectively placing AGNs in a

cosmological context (e.g., Mo & White 1996; Sheth & Tormen 1999). On smaller scales ($r_p \lesssim 1 h^{-1} \text{Mpc}$), clustering measurements estimate the fraction of AGNs that are hosted by satellite galaxies and place constraints on triggering and fueling from galaxy-galaxy interactions and mergers. Theoretical models that assume different internal or external AGN triggering mechanisms predict different large-scale clustering properties of AGNs, as a function of both luminosity and redshift (e.g., Silk & Rees 1998; Springel et al. 2005; Hopkins et al. 2006; Croton 2009; Hopkins & Hernquist 2009; Booth & Schaye 2010; Fanidakis et al. 2013; Hütsi et al. 2014). However, observational data suggest that only a weak luminosity dependence exists (e.g., Coil et al. 2009; Cappelluti et al. 2010; Krumpel et al. 2010; Allevalo et al. 2012; Koutoulidis et al. 2013). The measurement of clustering properties of AGNs across a range of redshifts and luminosities provides strong constraints to theoretical models of AGNs.

With the advent of the *XMM-Newton* and *Chandra* X-ray telescopes, early X-ray AGN clustering measurements at $z \sim 0.5$ – 2 targeted small fields and found that they reside in massive halos from $M_{\text{halo}} \sim 10^{12-13} h^{-1} M_{\odot}$ (Gilli et al. 2005; Yang et al. 2006). Later, Coil et al. (2009) measured the clustering of X-ray AGN sources at $z \sim 1$ with higher accuracy by using the cross-correlation of X-ray AGN sources with DEEP2 galaxies and using a larger field. They found that X-ray AGNs are more strongly clustered, similar to elliptical galaxies,

which are more clustered than star-forming galaxies. Generally, X-ray AGNs at $z \sim 1-2$ are more clustered than optically identified quasars as the same redshift and reside in relatively dense environments suggestive of being within group-like environments (e.g., Gilli et al. 2005; Puccetti et al. 2006; Yang et al. 2006; Coil et al. 2009; Hickox et al. 2009).

The NVSS (Condon et al. 1998) and FIRST (Becker et al. 1994) wide-area radio surveys identified large populations of luminous, low accretion rate, mechanically driven AGNs (e.g., Sijacki et al. 2007). Clustering studies using these radio AGNs found them to be strongly clustered, residing in very massive halos with $M_{\text{halo}} > 10^{13} h^{-1} M_{\odot}$ (Cress et al. 1996; Magliocchetti et al. 2004; Best et al. 2005). Hickox et al. (2009) studied the connection between AGNs selected using X-ray, radio, and mid-IR techniques by measuring the clustering, host properties, and AGN properties of sources in the Boötes field. They found that X-ray AGNs and radio AGNs reside in dark matter halos of mass $M_{\text{halo}} \sim 10^{13} h^{-1} M_{\odot}$ and $M_{\text{halo}} \sim 10^{13.5} h^{-1} M_{\odot}$, respectively, while IR-AGNs typically reside in lower mass halos with $M_{\text{halo}} < 10^{12} h^{-1} M_{\odot}$.

The observed differences in the clustering of X-ray AGN, radio AGN, and IR-AGN samples indicate that it is crucial to test for any obscuration dependence in AGN clustering. The simplest unified AGN models (e.g., Antonucci & Ulvestad 1985; Urry & Padovani 1995) would suggest that unobscured (type-1) and obscured (type-2) AGNs should have the same distribution of environments, with differences in the observed obscuration due only to the orientation of the AGNs relative to the observer. It has been suggested, however, that obscured and unobscured AGNs are similar objects observed at different evolutionary stages of SMBH accretion (e.g., Hopkins et al. 2008; Hickox et al. 2009). Most optical and X-ray AGN clustering studies do not find significant differences between the clustering of obscured and unobscured AGNs (e.g., Coil et al. 2009; Gilli et al. 2009). Hickox et al. (2011) found a marginal ($\sim 2\sigma$) increase in the clustering amplitude between obscured and unobscured IR-selected AGNs at $z \sim 1.25$, suggesting that obscured AGNs may reside in more massive halos. More recently, DiPompeo et al. (2014) and Donoso et al. (2014) found a significantly higher angular clustering amplitude for obscured compared to unobscured *Wide-field Infrared Survey Explorer* (WISE) AGNs at $z \sim 0.9$. However, these results measure only the angular projected clustering amplitude due to a lack of spectroscopic redshifts in their sample.

Selection biases inherent in AGN identification may also contribute to the observed clustering signals, in that radio AGNs are generally found in luminous, quiescent galaxies, X-ray AGNs are found in a mixture of quiescent and star-forming galaxies, and IR-AGNs are typically found in star-forming galaxies (e.g., Hickox et al. 2009; Aird et al. 2012; Mendez et al. 2013; Goulding et al. 2014). As quiescent galaxies are more strongly clustered than star-forming galaxies at a given redshift (e.g., Le Fèvre et al. 2005; Zehavi et al. 2005; Coil et al. 2008; Skibba et al. 2014), the observed clustering differences between AGNs selected at different wavelengths could be due in part to differences in their host populations. In order to understand the magnitude of this effect, one can compare the clustering of AGNs selected at different wavelengths to matched samples of inactive galaxies (e.g., Wake et al. 2008; Coil et al. 2009; Hickox et al. 2009; Mandelbaum et al. 2009). While Coil et al. (2009) found that X-ray AGNs are more clustered than color- and magnitude-

matched galaxy samples, Hickox et al. (2009) found that IR-AGNs are less clustered than color- and magnitude-matched samples. Interestingly, using weak lensing measurements at $z \sim 0.1$, Mandelbaum et al. (2009) found that dark matter halos of radio-loud AGNs are twice as massive as control galaxies of the same stellar mass and that radio AGNs are more clustered than optically selected AGNs.

In order to address these outstanding issues, here we measure the clustering properties of X-ray AGNs, radio AGNs, and IR-AGNs at $0.2 < z < 1.2$ using the DEEP2 and PRIMUS redshift surveys. The wealth of deep multi-wavelength data, combined with precise spectroscopic redshifts in these multiple fields, makes this sample both larger and deeper than similar previous studies at these redshifts. We use data from multiple fields, limiting the affect of cosmic variance. We measure the cross-correlation function of AGNs with dense galaxy samples, used to trace the large-scale structure in our fields. This leads to lower statistical errors than measuring the auto-correlation function of the AGNs directly. We investigate the dependence of clustering with intrinsic AGN properties (e.g., X-ray luminosity, specific accretion rate, hardness ratio, and obscuration). We create galaxy samples that are matched in stellar mass, star-formation rate (SFR), and redshift to the AGN samples identified in each wavelength, to compare the clustering of AGNs with similar inactive galaxies. This limits potential selection biases in comparing AGN samples selected at different wavelengths.

The paper is organized as follows. In Section 2 we present the spectroscopic redshift surveys and multi-wavelength data sets used here. In Section 3 we detail the different AGN selection techniques and the AGNs and galaxy samples used. In Section 5 we present the clustering measurements of the various AGNs and matched galaxy samples. We discuss our results in Section 6 and conclude in Section 7. Throughout the paper, we assume a standard flat Λ CDM model with $\Omega_m = 0.3$, $\Omega_{\Lambda} = 0.7$, and $H_0 = 72 \text{ km s}^{-1} \text{ Mpc}^{-1}$.

2. DATA

Our analysis combines multi-wavelength imaging with spectroscopic redshifts from the PRIMUS and DEEP2 galaxy redshift surveys, covering eight well known extragalactic fields: the CDFS-SWIRE field (Lonsdale et al. 2003), the COSMOS field (Scoville et al. 2007), the DEEP2 (DEEP2; Davis et al. 2003) 02 and 23 hr fields, as well as the Extended Groth Strip (EGS), the Elais-S1 (ES1) field (Oliver et al. 2000), and the XMM-Large Scale Structure field (XMM-LSS; Pierre et al. 2004). We describe the X-ray catalogs that we use in Section 2.1, the radio catalogs in Section 2.2, and the mid-IR catalogs in Section 2.3. In Sections 2.4 and 2.5 we briefly describe the PRIMUS and DEEP2 redshift surveys, respectively. In Section 2.6 we explain the methods used to estimate stellar masses and SFRs for PRIMUS and DEEP2 sources. In Section 2.7 we provide information on the spatial selection function of the PRIMUS and DEEP2 surveys that we use for our clustering analysis.

2.1. X-Ray Data

We use existing *Chandra* and *XMM-Newton* X-ray source catalogs of various depths in the COSMOS, DEEP2, ES1, EGS, and XMM-LSS fields (see Aird et al. 2012 and Mendez et al. 2013 for details). Due to the large positional uncertainty

Table 1
Field Information, Including Multi-wavelength Coverage Area and Number of Sources

Field	Area (deg ²)				Number of Detected Sources					
	X-ray	Radio	IRAC	WISE	$N_{\text{Galaxy}}^{\text{a}}$	$N_{\text{Mass}}^{\text{b}}$	$N_{\text{X-ray}}^{\text{c}}$	$N_{\text{Radio}}^{\text{d}}$	N_{Donley}	N_{Assef}
CDFS-SWIRE	...	1.77	1.77	1.77	20,423	20,380	...	37 (41)	131	44
COSMOS	0.93	0.93	0.93	0.93	12,284	12,265	203	94 (361)	45	27
Elais—South 1	0.51	0.90	0.90	0.90	9,922	9,903	67	64 (133)	59	18
Extended Groth Strip	0.69	0.71	0.61	0.71	13,957	13,178	343	43 (181)	64	15
DEEP2 02 hr	0.58	0.61	0.60	0.58	13,222	12,961	61	11 (11)	33	23
DEEP2 16 hr ^e	0.73	0.73	...	0.73	5,645	5,426	31	6 (6)	...	9
DEEP2 23 hr	0.89	0.92	...	0.67	13,486	13,239	75	9 (10)	...	19
XMM LSS/SXDS	2.88	2.88	2.84	2.88	35,460	35,388	178	78 (141)	157	79
Totals:	7.21	9.45	7.64	9.17	124,399	122,740	958	342 (894)	489	234

Notes.

^a Redshifts limited to $0.2 \leq z \leq 1.2$ and $z_{\text{quality}} \geq 3$.

^b Broadline AGNs are excluded, as the optical light for these AGNs is contaminated and prevents an accurate estimate of the stellar mass.

^c X-ray-detected sources with $L_X > 10^{41} \text{ erg s}^{-1}$.

^d Radio AGNs with $P_{1.4 \text{ GHz}} \geq 10^{24} \text{ Watts Hz}^{-1}$. The number within parentheses represents all detected radio sources with a robust redshift.

^e PRIMUS did not survey the DEEP2 16 hr field, and we include it only for samples at $0.7 < z < 1.2$.

of the X-ray point sources, we use the likelihood ratio matching technique (e.g., Sutherland & Saunders 1992; Ciliegi et al. 2003; Brusa et al. 2007; Laird et al. 2009) to identify optical counterparts to each X-ray source in each field. The likelihood ratio technique accounts for both the optical and X-ray positional uncertainties by calculating the probability of having a counterpart with a given magnitude above the probability of a spurious match. We place a lower limit on the positional uncertainty for the X-ray source location of $0''.5$ and require an optical match within $5''$ in any field. We restrict our sample to robust optical counterparts with likelihood ratios above >0.5 and choose the counterpart with the largest likelihood, when there are multiple counterparts. Table 1 lists the area of the X-ray coverage in each field, as well as the number of X-ray sources with redshifts (see Section 2.4 for details).

In the COSMOS field we use the public *XMM-Newton* X-ray point source catalog (Cappelluti et al. 2009; Brusa et al. 2010), which covers the entire 2 deg^2 to a depth of $f_{2-10 \text{ keV}} \sim 3 \times 10^{-15} \text{ erg s}^{-1} \text{ cm}^{-2}$. We further use the deeper *Chandra* point source catalog that has a depth of $f_{2-10 \text{ keV}} \sim 8 \times 10^{-16} \text{ erg s}^{-1} \text{ cm}^{-2}$ and covers the central $\sim 0.9 \text{ deg}^2$ (Elvis et al. 2009; Civano et al. 2012).

In the ES1 field, we use the Puccetti et al. (2006) point source catalog from four partially overlapping *XMM-Newton* pointings which has a depth of $f_{2-10 \text{ keV}} \sim 2 \times 10^{-15} \text{ erg s}^{-1} \text{ cm}^{-2}$ and covers 0.52 deg^2 of the PRIMUS area in this field.

We use the public X-ray point source catalog from the deep *Chandra* Advanced CCD Imaging Spectrometer (ACIS-I) XDEEP2 survey (Goulding et al. 2012) for the EGS and DEEP2-02 hr, DEEP2-16 hr, and DEEP2-23 hr fields. In the EGS, the XDEEP2 survey contains 96 *Chandra* pointings across the field, covering an area of 0.66 deg^2 . The typical full-band flux limit in the merged observations in this field is $f_X \sim 2.8 \times 10^{-16} \text{ erg s}^{-1} \text{ cm}^{-2}$, though this varies across the field due to the number of overlapping pointings. The DEEP2-02 hr, DEEP2-16 hr, and DEEP2-23 hr fields contain 12, 12, and 17 *Chandra* pointings respectively, with a full-band flux-limit of $f_X \sim 4.6 \times 10^{-15} \text{ erg s}^{-1} \text{ cm}^{-2}$ for all fields. In order to match the reported hard-band flux in the other fields, we convert the reported 2–7 keV hard X-ray band flux into an

equivalent 2–10 keV hard X-ray band flux assuming a $\Gamma = 1.9$ power law.

In the XMM-LSS field, we use the final release of the public XMM X-ray catalog from Chiappetti et al. (2013), which consists of 124 pointings of the *XMM-Newton* X-ray telescope which includes the Subaru XMM-Newton Deep Survey (SXDS; Ueda et al. 2008). This catalog contains sources to a hard-band flux limit of $f_X \sim 1.3 \times 10^{-15} \text{ erg s}^{-1} \text{ cm}^{-2}$ and $f_X \sim 9.3 \times 10^{-17} \text{ erg s}^{-1} \text{ cm}^{-2}$ in the shallower XMM-LSS and deeper XMM-SXDS regions, respectively. We match the X-ray catalogs using the likelihood ratio matching technique described above.

Following Aird et al. (2012) and Mendez et al. (2013), we apply an ‘‘X-ray weight’’ for each X-ray-detected source based on the ratio of the total number of X-ray-detected sources to the predicted $\log(N)$ – $\log(S)$ relation of Georgakakis et al. (2008) at a given flux. These X-ray weights correct the observed number densities of X-ray sources to the intrinsic number density and account for variations in the flux limit across the fields due to vignetting and the change in sensitivity of the telescope as a function of axis angle.

2.2. Radio Data

To select radio AGNs, we use existing deep Very Large Array (VLA) 1.4 GHz radio data in the COSMOS, EGS, and XMM-LSS fields. In the COSMOS field, we use the VLA-COSMOS Deep Project (Schinnerer et al. 2010), which combines the shallower data of the VLA-COSMOS Large Project (Schinnerer et al. 2007) with deeper coverage in the central degree of the field. The survey provides radio continuum coverage for ~ 2900 sources with $\sim 1''.5$ resolution and a mean 1σ sensitivity of $12 \mu\text{Jy beam}^{-1}$ in the central square degree and $\sim 2''$ resolution and sensitivity of $15 \mu\text{Jy beam}^{-1}$ in the outer region. In the EGS, we use the AEGIS20 (Iverson et al. 2007; Willner et al. 2012) VLA radio catalog which identifies 1122 sources from 6 overlapping pointings in the northern two-thirds of the field. The lower third of the EGS was not imaged due to the proximity to a bright radio source 3C 295. The data were obtained from the VLA with a 5σ sensitivity limit of $50 \mu\text{Jy beam}^{-1}$ with $\sim 3''.8$

resolution. In the XMM-LSS field, we use the 100 μJy catalog (Simpson et al. 2006), which contains 14 overlapping pointings. The radio imaging identifies 505 radio sources and reaches a sensitivity limit of 12 $\mu\text{Jy beam}^{-1}$ over 0.8 deg^2 of the field. In the DEEP2-02 hr, DEEP2-16 hr, and DEEP2-23 hr fields, we additionally include relatively shallow VLA data from the Faint Images of the Radio Sky at Twenty-one centimeters survey (FIRST; Becker et al. 1995). We use the 14Mar04 catalog which contains 946,432 radio sources above the sensitivity limit of $\sim 200 \mu\text{Jy beam}^{-1}$ and above the detection limit of 1 mJy.

We use the Australian Telescope Large Area Survey (ATLAS) in the CDFS-SWIRE field (Norris et al. 2006) and ES1 field (Middelberg et al. 2008). ATLAS used the Australian Telescope Compact Array (ACTA) at 1.4 GHz to survey both fields. The CDFS-SWIRE data contains 21 pointings with 784 radio galaxies reaching a 1σ sensitivity limit of $\sim 40 \mu\text{Jy beam}^{-1}$, while the ES1 data contains 12 pointings with 1276 radio galaxies reaching a 1σ sensitivity limit of $\sim 30 \mu\text{Jy beam}^{-1}$. We find no major astrometric offsets between these radio catalogs and the PRIMUS spectroscopic catalog (described below), such that we assign radio counterparts to the optical redshift catalog by using SPHEREMATCH in IDL to identify counterparts within $2''$, corresponding to the approximately astrometric uncertainty in the radio catalogs.

2.3. Mid-IR Data

To identify mid-IR-AGNs, we use existing public *Spitzer* IRAC photometry in the CDFS-SWIRE, COSMOS, EGS, ES1, and XMM-LSS fields. IRAC provides 3.6, 4.5, 5.8, and 8.0 μm data which we will reference as [3.6], [4.5], [5.8], and [8.0]. In the CDFS-SWIRE, ES1, and XMM-LSS fields we use existing shallow IRAC imaging from Data Release 2 (DR2) from the *Spitzer* Wide-area Infrared Extragalactic Survey (SWIRE; Lonsdale et al. 2003) (see Mendez et al. (2013) for details). We find no major astrometric offsets between these catalogs and the PRIMUS optical redshift catalog, and we assign IRAC counterparts to the optical redshift sources in all of the fields by matching to the closest object within $1''$. The CDFS “proper” field is not included here; instead, we use the larger CDFS-SWIRE field at slightly lower decl., which was covered by the PRIMUS survey. In the COSMOS field, we reproduce the SWIRE source detection procedure from the SWIRE DR2 documentation using the IRAC mosaic images (see Mendez et al. 2013 for details). This ensures that we measure robust fluxes and flux uncertainties using a consistent technique across all of our fields. For the majority of sources, our flux measurements are similar to those in the S-COSMOS public catalog, although the public catalog tends to have larger uncertainties for similar brightness objects from the SWIRE catalogs due to their aggressive deblending of sources.

In the DEEP2-02 hr field, we use a four-band-detected catalog.¹⁰ The sample is drawn from *Spitzer* IRAC observations as part of the DEEP2_CY5A/50660 program (PI: C. Jones). The IRAC imaging contains 34 pointings in each band, covering the majority of the DEEP-02 hr field. In the EGS field, we use the Barro et al. (2011) publicly available IRAC-[3.6]- and [4.5]-selected catalog. The catalog contains $\sim 76,000$ sources with $[3.6] \leq 23.75$. The sample is drawn from *Spitzer* as part of the Guaranteed Time Observations (GTO;

PI: G. Fazio) and presented in Barmby et al. (2008) with additional data from the GO program (ID 41023; PI: K. Nandra). The GTO IRAC imaging comprises 52 pointing of all 4 IRAC bands over the central region of the EGS. The additional GO data cover the upper and lower regions of the EGS, flanking the original strip.

Additionally, we use data from *WISE* (Wright et al. 2010), which provides 3.4, 4.5, 12, and 22 μm photometry (bands W1, W2, W3, and W4, respectively) in all of our fields. Here we use the public all-sky catalog from March 2012 which has a 5σ point source sensitivity better than 0.08, 0.11, 1, and 6 mJy in each of the bands, respectively. We remove sources with spurious photometric detections and require sources to have signal-to-noise ratio (S/N) > 3 in the W1 and W2 bands (see Cutri et al. 2012 for more details). *WISE* surveyed the sky in an ecliptic polar orbit, which increased the number of observations with increasing ecliptic latitude, causing the median coverage to vary for different fields. See Table 1 for the IRAC and *WISE* area (where at least W1 and W2 photometry was required) of each field.

2.4. PRIMUS Spectroscopic Redshifts

We use spectroscopic redshifts from the PRIMUS redshift survey to define samples for our clustering analysis. PRIMUS (Coil et al. 2011; Cool et al. 2013) is the largest faint galaxy redshift survey completed to date, covering $\sim 9 \text{deg}^2$ in seven well studied fields on the sky with multi-wavelength imaging from the X-ray to the far-infrared (IR). The survey obtained low-resolution ($\lambda/\Delta\lambda \sim 40$) spectra for $\sim 300,000$ objects, targeting 80% of galaxies in these fields with $i < 22$. PRIMUS used the IMACS instrument (Bigelow & Dressler 2003) on the *Magellan-I* Baade 6.5 m telescope to observe $\sim 2,500$ objects at once using a slitmask that covered 0.18 deg^2 . PRIMUS contains a statistically complete sample of $\sim 120,000$ spectroscopic redshifts to $i_{\text{AB}} \sim 23.5$. Redshifts are derived by fitting a large suite of galaxy, broadline AGNs (BLAGNs), and stellar spectral templates to the low-resolution spectra and optical photometry (see Cool et al. 2013 for details). Objects are classified as galaxies, BLAGNs, or stars depending on the best χ^2 template fit. The PRIMUS redshifts are very precise ($\sigma_z/(1+z) \sim 0.5\%$) and have a low catastrophic outlier rate, less than 3% ($\Delta z/(1+z) \geq 0.03$). Here we use robust ($z_{\text{quality}} \geq 3$; see Coil et al. 2011) PRIMUS redshifts between $0.2 < z < 1.2$ for the fields listed in Table 1. For further details of the survey design, targeting, and data, see Coil et al. (2011); for details of the data reduction, redshift confidence, and completeness, see Cool et al. (2013).

The PRIMUS survey generally targeted all sources above $i < 22.5$ and sparse-sampled $22.5 < i < 23$ sources, so that faint galaxy sources at the flux limit would not dominate the target selection. The sampling rates are well defined a priori such that building a statistically complete flux-limited sample requires the tracking of both the “sparse sampling” weight and the “density-dependent” weight of each object. The magnitude-dependent sparse sampling weight accounts for the fraction of sources selected at random in the 0.5 mag interval above the targeting limit in each field. The density-dependent weight accounts for the sources in high density areas on the sky that are missed due to slit collisions and the finite number of masks observed. In these regions the observed spectra of adjacent galaxies would overlap on the detector if all galaxies were

¹⁰ Catalog from A. Goulding (2013, private communication).

targeted (see Coil et al. 2011; Moustakas et al. 2013, for more details).

Additionally, here we include a spatially varying redshift success fraction weight to account for changes in the observed redshift success rate across a field (i.e., due to differences in observing conditions for different slitmasks). In the PRIMUS field we use the `pixelize` function in `Mangle`.¹¹ We estimate the redshift success fraction by taking the ratio of highly confident sources with $z_{\text{quality}} \geq 3$ to all targeted sources in the field in pixels of size $\sim 36 \text{ arcsec}^2$. We use a larger pixel size in the PRIMUS fields than in the DEEP2 fields (see Section 2.5) to limit Poisson noise in the shallower PRIMUS data.

The inclusion of these targeting and completeness weights is important, as they correct the observations to more accurately represent the full galaxy population. However, the $i \sim 23.5$ selection corresponds to a rest-frame selection $\sim 5000 \text{ \AA}$ at $z = 0.7$, such that at the highest redshifts we are incomplete for fainter, red galaxies. The redshift completeness is only a weak function of the color of galaxies and is a stronger function of luminosity (Cool et al. 2013). For the purposes of this paper, we compare the clustering of AGN samples either with each other or with matched galaxy samples, and these weights are applied to all samples.

2.5. DEEP2 Spectroscopic Redshifts

We also use spectroscopic redshifts from the Deep Extragalactic Evolutionary Probe (DEEP2; Davis et al. 2003; Newman et al. 2013) redshift survey. In the DEEP2-02 hr and DEEP2-23 hr fields, PRIMUS did not target the $0.7 < z < 1.4$ redshift range already covered by DEEP2. The combination of PRIMUS redshifts and DEEP2 redshifts in these fields selects galaxies uniformly from $z = 0.2$ to $z = 1.4$. The DEEP2 survey provides spectroscopic redshifts in the EGS, the DEEP2-02 hr field, the DEEP2-16 hr field, and the DEEP2-23 hr field. The DEEP2 survey was conducted with the DEIMOS spectrograph (Faber et al. 2003) on the 10 m Keck II telescope. In the EGS, the DEEP2 survey has measured $\sim 17,000$ high-confidence redshifts ($Q \geq 3$; see Newman et al. 2013) to $R_{AB} = 24.1$. In the DEEP2-02 hr, DEEP2-16 hr, and DEEP2-23 hr fields, the survey used a photometric color selection to target galaxies at $0.7 < z < 1.4$ to $R_{AB} = 24.1$. We use the Data Release 4 (DR4) catalog¹² and associated window function from (Newman et al. 2013). Here we use redshifts between $0.2 < z < 1.2$ in the EGS and redshifts between $0.7 < z < 1.2$ in the other DEEP2 fields. For all of the DEEP2 fields, we require a redshift with a confidence greater than 95% ($Q \geq 3$). We use the extended optical photometry from Matthews et al. (2013) which contains additional Canada–France–Hawaii Telescope Legacy Survey (CFHTLS) *ugriz* and the Sloan Digital Sky Survey (SDSS) *ugriz* photometry matched to the redshift catalog. K-corrections, absolute M_B magnitudes, and rest-frame colors are derived from K-correct (Blanton & Roweis 2007) from the optical photometry in these fields. The numbers of sources with the above redshift quality cuts and with estimated stellar masses are given in Table 1.

We use those sources that fall within the recoverable spatial selection function of the DEEP2 survey. For the EGS, this precludes the use of the data from the northern 25% of the field,

which had shallower BRI photometry and non-uniform targeting. For the other DEEP2 fields, we include all of the pointings presented in Newman et al. (2013). The spatial redshift success fraction reflects the probability that a targeted source has a secure $z_{\text{quality}} \geq 3$ redshift. For the DEEP2 fields, we calculate this in $\sim 6 \text{ arcsec}^2$ pixels. Using the average of six adjacent pixels to match the $\sim 36 \text{ arcsec}^2$ pixels used in PRIMUS does not change the resulting clustering measurements in these fields.

2.6. iSEDfit Stellar Masses and SFRs

We estimate stellar masses and SFRs by fitting the spectral energy distributions (SEDs) of our sources with population synthesis models using `iSEDfit` (Moustakas et al. 2013). `iSEDfit` is a Bayesian fitting code that compares the observed photometry for each source to a large Monte Carlo grid of SED models which span a wide range of stellar population parameters (e.g., age, metallicity, and star-formation history) to estimate the stellar mass and SFR of a galaxy. We assume a Chabrier (2003) initial mass function from 0.1 to $100 M_{\odot}$ and use Bruzual & Charlot (2003) stellar population synthesis models. We assume the following priors to construct the Monte Carlo grids: uniform stellar metallicity in the range of $0.004 < Z < 0.04$; Charlot & Fall (2000) dust attenuation law, with an exponential distribution of dust, ($0.25 < \gamma < 2.0$); an exponentially declining- τ ($\phi_{\lambda}(t) = (M/\tau)e^{-t/\tau}$) star-formation history (SFH) with $0.01 < \tau < 5.0$. Stochastic bursts of star formation of varying amplitude, duration, and onset time are superimposed, allowing for a wide range of possible star-formation histories (Kauffmann et al. 2003; Salim et al. 2007). While a delayed- τ model encompasses both a linearly rising ($t/\tau \ll 1$) and an exponentially declining ($t/\tau \gg 1$) SFH history, we find no significant SFR or stellar mass offsets or trends using different SFH models for our sources at $z < 1.2$, and we therefore choose to use a simpler model of an exponentially declining SFH. `iSEDfit` marginalizes the full posterior probability distribution of stellar masses and SFRs over all other parameters and thus encapsulates both the uncertainties in the observations and the model parameter degeneracies. For each source, we take the median stellar mass and SFR from the full probability distribution functions as the best estimate of the stellar mass and SFR. The median uncertainties on the log stellar mass and SFR are 0.08 dex and 0.2 dex, respectively. In our analysis below, we are primarily interested in the relative stellar mass and SFR between sources, such that any overall offsets do not affect our results.

We use `iSEDfit` stellar masses derived from photometry spanning the UV to the optical bands. Including the first two IRAC bands ([3.6] and [4.5]) systematically increases the median galaxy sample stellar mass by 0.1 dex. This is also the case for the X-ray-detected sample; however, for the IRAC Donley et al. IR-AGN-selected sample (details are given below in Section 3.3), the median mass offset is much larger (0.5 dex). As shown in Mendez et al. (2013), this is due to AGN light contributing to these channels causing the IR-AGNs to have overestimated stellar masses. We therefore do not include the IRAC bands in any of our stellar mass estimates, such that all stellar masses are derived using the same photometric bands, minimizing systematic offsets between our samples. As $\sim 82\%$ of the area covered by PRIMUS has *GALEX* UV coverage, we include the observed FUV and NUV photometry where

¹¹ <http://space.mit.edu/~molly/mangle/>

¹² <http://deep.ps.uci.edu/dr4/home.html>

available to improve the SFR estimates. Including the *GALEX* UV bands (compared to just using optical bands alone) slightly decreases the estimated stellar mass (~ 0.02 dex) for the galaxy and AGN samples. We do not estimate stellar masses or SFRs for sources that are deemed to be BLAGNs, where their spectra are better matched by BLAGN templates than by galaxy templates, as their optical photometry will be dominated by light from the AGNs. Table 1 lists the total number of sources with spectroscopic redshifts in each field (N_{galaxy}) and the number of sources for which we estimate a stellar mass (N_{mass}) and SFR.

Azadi et al. (2015) investigate how the PRIMUS SFR estimates derived using SED fits compare with estimates using $100\ \mu\text{m}$ data for those galaxies detected with *Herschel*. They find that a histogram of the SED to *Herschel*-based SFR differences peaks at zero, though there is a non-symmetric tail to higher SFR estimates using the *Herschel* data, such that the median difference is 0.6 dex. Most galaxies and AGNs are not *Herschel*-detected, such that the typical difference for the full sample could be smaller, as *Herschel* detections are biased toward more dusty sources. However, in this paper we are concerned only with *relative* SFRs, such that any overall offsets in the SFR estimates will not change our results.

2.7. Spatial Selection Function

In order to perform accurate clustering measurements, we require that all of the PRIMUS and DEEP2 sources used here are located within the area of each survey that has a well understood spatial selection function. This ensures that any spatially dependent density differences in the surveys that are due to target selection or missing data, such as in CCD chip gaps or around bright stars, as well accounted for. In PRIMUS we require that sources fall within the observed window function area targeted with at least two slitmasks. Coil et al. (2011) provides details on the spatial selection function of PRIMUS, and Coil et al. (2004) and Newman et al. (2013) provide details for the DEEP2 survey. The X-ray AGN, radio AGN, and IR-AGN samples are identified within the areas with observed X-ray, radio, or mid-IR coverage. While there is generally overlap between the multi-wavelength imaging coverage, there are some areas that lack full multi-wavelength coverage.

3. AGN AND GALAXY SAMPLES

The goal of this paper is to quantify and compare the clustering properties of X-ray-, radio-, and mid-IR-selected AGNs at $z \sim 0.7$ with each other, as well as with inactive galaxies with stellar mass, SFR, and redshift distributions that match the AGN samples. To this end, we select AGNs and galaxy samples using the PRIMUS and DEEP2 surveys in regions with either X-ray, radio, or mid-IR imaging coverage. Below we present our selection criteria for our AGNs and matched galaxy samples. Details of each AGN sample are given in Table 2.

3.1. X-Ray AGN Samples

For the fiducial X-ray AGN sample, we require that the detected X-ray sources have a hard-band X-ray luminosity $L_X > 10^{41}\ \text{erg s}^{-1}$ and a redshift in the range $0.2 < z < 1.2$. We choose to use an X-ray luminosity limit of $L_X > 10^{41}\ \text{erg s}^{-1}$ rather than a more conservative

$L_X > 10^{42}\ \text{erg s}^{-1}$ limit, as this leads to larger samples with smaller uncertainties and no significant differences in our results. We have applied X-ray K-corrections ($(1+z)^{\Gamma-2}$; $\Gamma \sim 1.7$) to estimate the hard-band X-ray luminosity. We create a “non-broadline” subsample where we remove the sources identified as BLAGNs in their PRIMUS or DEEP2 spectra. The fiducial X-ray AGN sample is additionally divided into six subsamples defined either by an AGN property (L_X , specific accretion rate, or hardness ratio) or a host galaxy property (redshift, stellar mass, or specific star-formation rate; sSFR), in order to investigate clustering trends with both AGNs and host galaxy properties.

For the X-ray AGN samples split by AGN luminosity, we divide the fiducial X-ray AGN sample into low-luminosity ($\langle L_X \rangle \sim 10^{42.4}\ \text{erg s}^{-1}$) and high-luminosity ($\langle L_X \rangle \sim 10^{43.2}\ \text{erg s}^{-1}$) samples using a luminosity cut, shown in the upper left panel of Figure 1.

We also split the fiducial X-ray AGN sample by specific accretion rate, defined as

$$\lambda_{\text{Edd}} = \frac{L_{\text{Bol}}}{L_{\text{Edd}}} \quad (1)$$

$$= \frac{L_{\text{Bol}}}{1.3 \times 10^{38}\ \text{erg s}^{-1} \times 0.002 \frac{\mathcal{M}_*}{\mathcal{M}_\odot}}, \quad (2)$$

where L_{Edd} is the Eddington limit, and L_{Bol} is the bolometric luminosity derived using the X-ray luminosity to bolometric luminosity relationship of Hopkins et al. (2008) in units of erg s^{-1} . The specific accretion rate is a rough estimate of the Eddington ratio, assuming a constant scaling relationship between black hole mass and host stellar mass (e.g., $\mathcal{M}_{\text{BH}} \sim 0.002 \mathcal{M}_*$; Marconi & Hunt 2003). While there is substantial scatter in both the M - σ relationship and in the scaling between bulge mass and stellar mass of the galaxy, such that the specific accretion rate is not an exact estimate of the Eddington ratio, it is a robust tracer of the rate at which the SMBH is growing relative to the stellar mass of the host galaxy (Aird et al. 2012).

We create high and low specific accretion rate (λ) samples only for AGNs with a host galaxy stellar mass above the stellar mass limit ($\mathcal{M}_* = 10^{9.75} \mathcal{M}_\odot$) for which we are complete for quiescent galaxies at the highest redshifts used here and divide the fiducial X-ray sample at roughly the median specific accretion rate of $\lambda = 10^{-2}\ \text{erg s}^{-1} \mathcal{M}_\odot^{-1}$ (see the lower right panel of Figure 1). We also create X-ray AGN samples based on hardness ratio, defining hard and soft samples by dividing the fiducial sample at $\text{HR} = 0$ and requiring that the AGNs included are identified in both the soft and hard X-ray bands. We adopt a simple cut of $\text{HR} = 0$ as this approximately corresponds to $N_{\text{H}} = 3 \times 10^{22}\ \text{cm}^{-2}$, assuming a simple absorbed power-law X-ray spectrum with $\Gamma = 1.9$ at $z = 0.6$ (the approximate median redshift of our sample), and thus roughly divides the sample into obscured and unobscured populations (Szokoly et al. 2004; Hasinger 2008).

We further divide the fiducial X-ray AGN sample by various host galaxy properties, to quantify how the clustering of X-ray AGNs depends on the host galaxy. We create a high- and low-redshift sample by dividing the fiducial X-ray AGN sample at $z \sim 0.7$. For both the stellar mass samples and sSFR samples, we require that the host galaxy has a stellar mass above

Table 2
Information on the X-Ray, Radio, and IR-AGN Samples

AGN Selection	Sample Name	Redshift Range	Number ^a	Density ^b	$\langle z \rangle$	$\langle L \rangle^c$	$\langle M_* \rangle^d$
X-ray AGN	Full	0.2–1.2	958	0.79	0.73	42.8	10.7
Radio AGN	Full	0.2–1.2	894	0.55	0.62	23.5	10.9
Donley IR-AGN	Full	0.2–1.2	583	0.44	0.68	44.2	10.5
X-ray AGN	Non-broadline	0.2–1.2	633	0.53	0.72	42.7	10.8
Radio AGN	Non-Broadline	0.2–1.2	768	0.48	0.61	23.5	10.91
Donley IR-AGN	Non-broadline	0.2–1.2	328	0.25	0.61	44.0	10.4
X-ray AGN	Low L_X	0.2–1.2	288	0.26	0.57	42.2	10.7
X-ray AGN	High L_X	0.2–1.2	328	0.33	0.87	43.3	10.8
X-ray AGN	Low λ	0.2–1.2	329	0.27	0.65	42.4	10.9
X-ray AGN	High λ	0.2–1.2	305	0.26	0.90	43.4	10.7
X-ray AGN	Low HR	0.2–1.2	671	0.54	0.73	42.9	10.7
X-ray AGN	High HR	0.2–1.2	287	0.25	0.73	42.7	10.8
Radio AGN	High $P_{1.4 \text{ GHz}}$	0.2–1.2	327	0.21	0.80	24.3	11.2
Radio AGN	Low $P_{1.4 \text{ GHz}}$	0.2–1.2	569	0.34	0.50	23.3	10.8
Assef IR-AGN	Full	0.2–1.2	234	0.14	0.74	44.5	10.6
Assef IR-AGN	Obscured <i>WISE</i> color	0.2–1.2	129	0.08	0.77	44.5	10.6
Assef IR-AGN	Unobscured <i>WISE</i> color	0.2–1.2	106	0.06	0.70	44.5	10.6

Notes.

^a Number of sources in window function with applied selection cuts.

^b Density is in units of $[10^{-4} h^3 \text{ Mpc}^{-3}]$.

^c $\langle L \rangle$ is $\langle L_X \rangle$ [$\log(\text{erg s}^{-1})$] for X-ray AGN samples, $\langle P_{1.4 \text{ GHz}} \rangle$ [$\log(\text{Watts Hz}^{-1})$] for radio AGN, and $\langle L_{3.6 \mu\text{m}} \rangle$ [$\log(\text{erg s}^{-1})$] for IR-AGN samples.

^d Units of $[\log(h^{-1} M_\odot)]$.

$M_* = 10^{9.75} M_\odot$ (see Figure 2). We define the high and low stellar mass samples using the median stellar mass of the fiducial X-ray AGN sample ($M_* \sim 10^{10.65} M_\odot$), and we define high and low sSFR samples by dividing the sSFR at $\text{sSFR} = 10.65 \text{ years}^{-1}$ (see Figure 2). This cut roughly matches the evolving mass dependent SFR cut of Moustakas et al. (2013) at $z \sim 0.7$ that divides the galaxy sample into quiescent and star-forming galaxies.

3.2. Radio AGN Samples

We define four radio AGN samples based on the observed optical broad lines and measured radio luminosity of each source. For our fiducial radio AGN sample, we require $0.2 < z < 1.2$. We create a “non-broadline” subsample where we remove the BLAGNs identified by their PRIMUS or DEEP2 optical spectra. We have applied a radio K-correction $((1+z)^{\alpha-1})$; $\alpha \sim 0.5$) when estimating the radio luminosity. Radio continuum emission may contain contributions from thermal bremsstrahlung (free-free) emission in star-forming galaxies as well as from non-thermal synchrotron emission associated with radio jets emanating from an AGN. To separate these two populations, we follow Condon (1992) and Murphy et al. (2011) and define a high-luminosity radio sample with $P_{1.4 \text{ GHz}} > 10^{24} \text{ Watts Hz}^{-1}$ to remove any potential contamination from luminous starburst galaxies. Above this luminosity, the radio emission cannot be explained by even extreme star formation ($\text{SFR} > 10^3 M_\odot \text{ yr}^{-1}$; Goulding et al. 2012; Hickox et al. 2009). This radio AGN sample reliably contains radio-loud (Class FR-II; Fanaroff & Riley 1974) sources. The small sample size in the high-

luminosity sample limits our analysis of the radio AGN sample to the fiducial redshift range ($0.2 < z < 1.2$), as we do not have enough sources to create subsamples at different redshifts.

This sample of radio-loud sources necessarily does not contain radio-quiet AGNs (Mullaney et al. 2013). A variety of optical, mid-IR, or far-IR to radio flux ratio excess techniques have been suggested to identify more complete samples of radio-quiet AGNs while limiting contamination from star-forming galaxies (e.g., Appleton et al. 2004; Donley et al. 2005; Park et al. 2008; Smolčić et al. 2008). To investigate the clustering properties of radio-quiet AGNs, we define a low-luminosity radio sample ($P_{1.4 \text{ GHz}} < 10^{24} \text{ Watts Hz}^{-1}$). This sample includes all radio-detected sources below the luminosity limit, identifying all possible optical- or IR-excess selected sources.

In order to investigate possible contamination of this low-luminosity radio sample by star-forming galaxies, in the upper panel of Figure 3 we show SFR versus radio luminosity for the radio-detected sample. We highlight high-luminosity ($P_{1.4 \text{ GHz}} > 10^{24} \text{ Watts Hz}^{-1}$) sources in red, X-ray AGNs that are radio-detected in green, and Donley et al. IR-AGNs that are radio-detected in blue. The radio luminosity distribution of the X-ray AGN and Donley et al. IR-AGN samples are shown as normalized histograms at the bottom of the panel. Cyan points highlight the few highly star-forming sources where their radio luminosity can be explained solely as due to star formation using the Murphy et al. (2011) SFR-to-radio luminosity relationship (purple line). The small number of sources ($\lesssim 1\%$) above this line shows that neither the high- nor low-luminosity radio samples are contaminated by star-forming

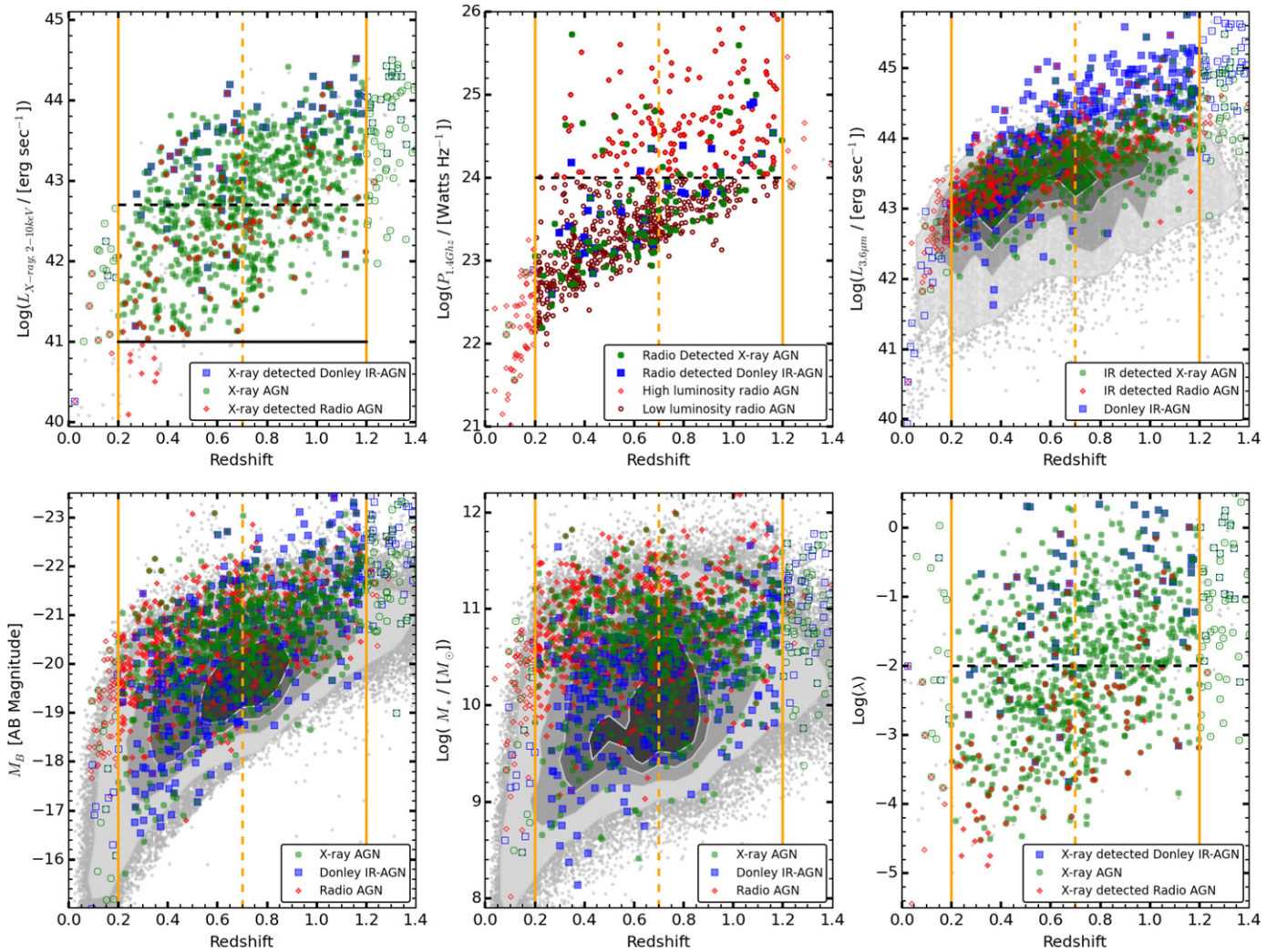


Figure 1. Distributions of X-ray AGNs, radio AGNs, and Donley et al. IR-AGNs in X-ray AGN luminosity (upper left), radio power (upper center), and $3.6 \mu\text{m}$ IR luminosity (upper right), as well as host galaxy absolute optical magnitude (M_B ; lower left), stellar mass (lower center), and X-ray specific accretion rate (lower right), all as a function of redshift for $0 < z < 1.4$. X-ray AGNs are shown with green circles, radio AGNs with red diamonds, and Donley et al. IR-AGNs with blue squares, along with inactive galaxies shown as gray dots with grayscale contours containing 30%, 50%, and 80% of the full sample. Sources shown here have robust spectroscopic redshifts and are not classified as broadband AGNs. Solid vertical orange lines show the full redshift range used here ($0.2 < z < 1.2$), while the dashed vertical orange line shows the redshift used ($z = 0.7$) to split the full samples into higher and lower redshift samples. In the upper left panel, we show a dashed black line for the X-ray luminosity cut used to create high and low X-ray luminosity samples, while the solid black line shows the lower $L_X = 10^{41} \text{ erg s}^{-1}$ luminosity cut used for all of the X-ray AGN samples. In upper center panel, the dashed black line shows the $P_{1.4 \text{ GHz}} = 10^{24} \text{ Watts Hz}^{-1}$ luminosity cut that we use to create high- and low-luminosity radio samples. In the lower right panel, we show a dashed black line for the specific accretion rate cut used to create high and low specific accretion rate samples. Donley et al. IR-AGNs tend to have higher X-ray and IR luminosities compared to X-ray AGN and radio AGN sources.

galaxies. The median uncertainty on the SFR estimates is less than 0.2 dex, suggesting that only a few sources could be scattered above the Murphy et al. (2011) line. We also find that most of the X-ray and mid-IR-AGNs that are radio-detected are in the low-luminosity radio sample $P_{1.4 \text{ GHz}} < 10^{24} \text{ Watts Hz}^{-1}$, supporting the conclusion of minimal contamination from star-forming galaxies.

In the bottom panel of Figure 3 we show the sSFR versus stellar mass diagram for all PRIMUS galaxies (gray contours), low-luminosity (black points), and high-luminosity radio AGNs ($P_{1.4 \text{ GHz}} > 10^{24} \text{ Watts Hz}^{-1}$, red points). Radio-detected sources are preferentially identified in massive galaxies, with the high-luminosity sources found in the most massive galaxies. We do not find large differences in the sSFRs of the low-luminosity radio sources compared to the high-luminosity radio sources.

3.3. IR-AGN Samples

We use the Donley et al. (2012) IRAC color-color selection to identify mid-IR red power-law AGNs. As shown in Mendez et al. (2013), in the PRIMUS survey this selection provides reliable identification of luminous AGNs with minimal contamination by star-forming galaxies. We require that objects are detected in all four IRAC bands and have colors such that they lie within the following region in IRAC color-color space:

$$x = \log_{10} \left(\frac{f_{5.8 \mu\text{m}}}{f_{3.6 \mu\text{m}}} \right), \quad y = \log_{10} \left(\frac{f_{8.0 \mu\text{m}}}{f_{4.5 \mu\text{m}}} \right) \quad (3)$$

$$x \geq 0.08 \text{ and } y \geq 0.15 \text{ and} \quad (4)$$

$$y \geq (1.21 \times x) - 0.27 \text{ and} \quad (5)$$

$$y \leq (1.21 \times x) + 0.27 \text{ and} \quad (6)$$

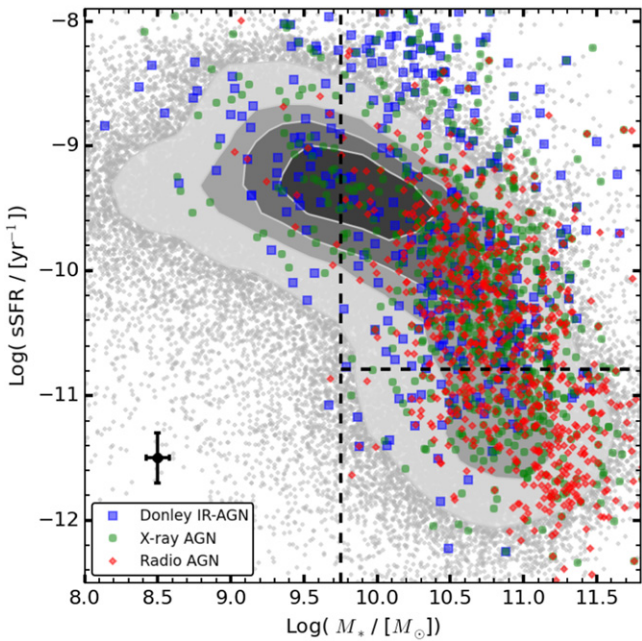


Figure 2. Specific star-formation rate (sSFR) vs. stellar mass for the X-ray AGN, radio AGN, and Donley et al. IR-AGN sources. Colors and contours are similar to Figure 1. Dashed black lines show the stellar mass and sSFR cuts used to define the sSFR-selected samples. AGNs identified at different wavelengths have different distributions in both sSFR and stellar mass, though AGNs identified at any wavelengths are typically identified in massive host galaxies. Median 1σ errors on both parameters are shown in the lower left corner.

$$f_{4.5\mu\text{m}} > f_{3.6\mu\text{m}} \text{ and } f_{5.8\mu\text{m}} > f_{4.5\mu\text{m}} \text{ and} \quad (7)$$

$$f_{8.0\mu\text{m}} > f_{5.8\mu\text{m}}. \quad (8)$$

The small sample size of the Donley et al. IR-AGN sample limits our analysis to the fiducial redshift range ($0.2 < z < 1.2$).

Additionally, we identify *WISE*-selected IR-AGNs using the Assef et al. (2013) magnitude-dependent selection. We require sources to have measured W1 and W2 fluxes such that,

$$W1 - W2 > 0.662 \exp[0.232 (W2 - 13.97)^2] \quad (9)$$

$$W2 < 17.11, \quad (10)$$

where W1 and W2 are in Vega magnitudes. Assef et al. (2013) show that this selection is 90% reliable in its identification of IRAC-selected AGNs. This selection extends the Stern et al. (2012) *WISE* IR-AGN color selection to fainter limiting magnitudes, while controlling for contamination (see Assef et al. 2013 for details).

In Figure 4 we compare the MIR colors of Donley et al. IR-AGNs and Assef et al. IR-AGNs. In the top panel we show the *WISE* selection plane with the Mateos et al. (2012) color-color selection wedge in orange and the Stern et al. (2012) unobscured color selection limit in red. We show *WISE*-detected Donley et al. IR-AGNs with blue points, Assef et al. IR-AGNs with red points, and PRIMUS galaxies with gray contours and gray outlier points. In this color-color space, the Donley et al. IR-AGNs and Assef et al. IR-AGNs generally have similar MIR colors, with the Donley et al. IR-AGNs extending to slightly lower [W1-W2] colors. In the bottom panel, we show the IRAC color-color selection wedge with the Stern et al. (2005) selection in orange and the power-law locus in red. We

show Donley et al. IR-AGNs with blue points, Assef et al. IR-AGNs that are IRAC-detected with red points, and the PRIMUS galaxy sample in gray contours. We find that some Assef et al. IR-AGNs have high IRAC [Ch3-Ch4] colors, beyond the Stern et al. (2005) wedge and power-law locus. This results from the Assef et al. IR-AGN selection using only the two shorter wavelength *WISE* bands and not using the longer wavelength information. These few sources are likely not AGNs as they reside in the region of this diagram dominated by low-redshift ($z \lesssim 0.3$), star-forming galaxies (Mendez et al. 2013). The Donley et al. IR-AGN selection uses all four bands to ensure a red monotonically increasing flux in the MIR, at the cost of requiring detections in the generally shallow longer wavebands.

We divide the *WISE* IR-AGN sample into obscured and unobscured subsamples. We use the criteria of Yan et al. (2013), who use obscured and unobscured templates at $z < 1.5$, to define a MIR-to-optical color cut of $(r - W2) \sim 6$ to separate these sources. Due to differences in the photometric filters in our measured r-band magnitudes, we use a synthesized SDSS r-band magnitude from *K-Correct* to ensure a uniform selection in each field. In the top panel of Figure 5 we show the selection of our samples in the optical and MIR color-color diagram, where obscured Assef et al. IR-AGNs are shown in red and unobscured Assef et al. IR-AGNs in blue. In the bottom panel, we show the optical-to-MIR color distributions of the obscured (red) and unobscured (blue) samples, as well as the optically identified broadline AGNs (black) in these samples. We find that most broadline AGNs have colors that identify them as unobscured AGNs.

We additionally test the Mateos et al. (2012) *WISE* IR selection technique. Similar to the Donley et al. IR-AGN selection, it identifies sources with a red power law in the mid-IR. This technique is more robust than that of Assef et al. (2013) as it uses longer wavelength information (W3: $12\mu\text{m}$) to ensure a monotonic mid-IR SED, but it is less complete due to the relatively shallow W3 coverage in the *WISE* survey. As we find no significant differences in the clustering properties of the AGN samples defined using Mateos et al. (2012) and Assef et al. (2013), we use the slightly larger Assef et al. IR-AGN sample throughout this paper.

3.4. Galaxy Tracer Samples

We use the dense galaxy samples provided by the PRIMUS and DEEP2 redshift surveys to measure the clustering of AGNs using a cross-correlation measurement with galaxies. To do this, we define galaxy “tracer” samples to trace the cosmic web in the fields and at the redshifts of interest. For the fiducial galaxy tracer sample, we use all galaxies with robust redshifts within the fiducial redshift range used here, $0.2 < z < 1.2$. We do not require that the galaxy tracer sample be volume-limited, as we are using it only to trace the large-scale structure in these fields; it therefore needs to span the same volume as our AGN samples, but it does not need to have the same median luminosity at all redshifts. We additionally split the fiducial galaxy tracer sample into low- and high-redshift subsamples for the X-ray AGN sample, split at the redshift of $z = 0.7$ (Figure 1, dashed orange line in each panel). This redshift cut divides the number of X-ray AGNs into approximately equal-sized samples and results in 30% more tracer galaxies at lower redshifts than at higher redshifts.

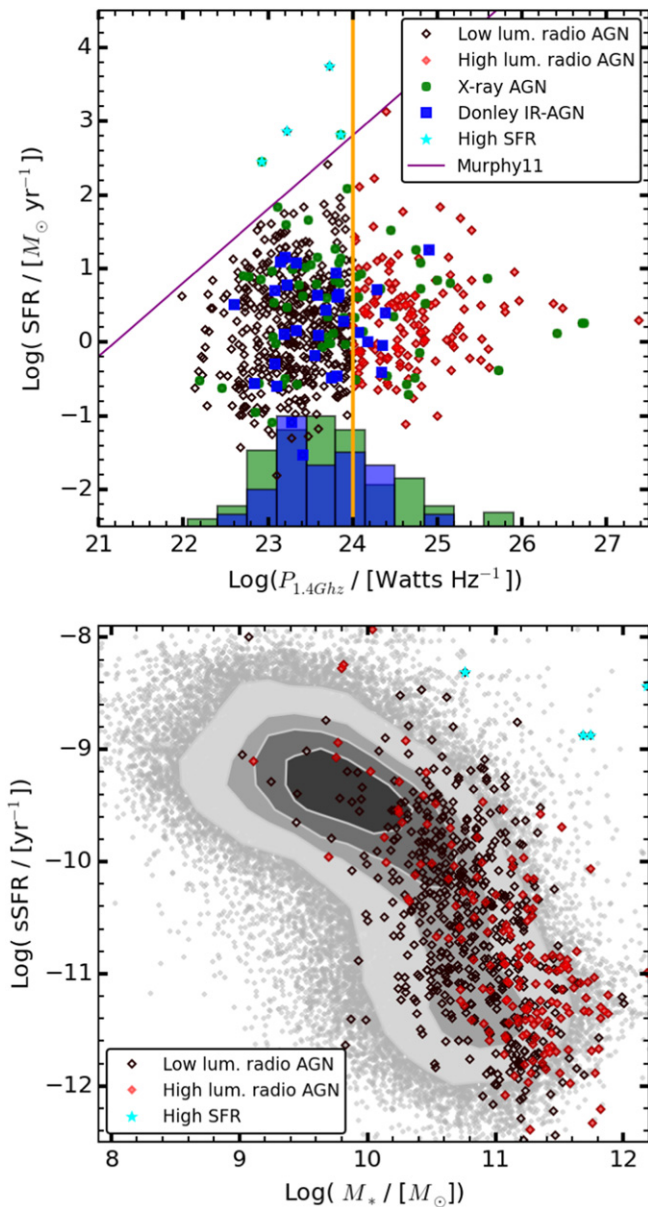


Figure 3. Host galaxy properties for radio AGNs. Top: SFR vs. radio luminosity for the fiducial radio-detected sample. High-luminosity ($P_{1.4\text{GHz}} > 10^{24}$ Watts Hz^{-1}) radio AGNs are highlighted as red points. X-ray AGNs and Donley et al. IR-AGNs that are radio-detected are shown with green and blue points, respectively, with relative distributions shown at the bottom. Radio AGNs above the Murphy et al. (2011) SFR-to-radio luminosity relationship (purple line) are highlighted in cyan. In only these four sources can the radio light be dominated by star formation and not AGN activity. Bottom: comparison of low-luminosity (black) and high-luminosity (red) radio AGNs in the sSFR and stellar mass plane. The PRIMUS galaxy sample is shown in gray contours, with outliers beyond the 90% contour shown with gray points. The four sources above the SFR-to-radio luminosity relationship of Murphy et al. (2011) are shown as cyan points.

3.5. Galaxy-matched Control Samples

We construct galaxy samples for each of the fiducial X-ray AGN, radio AGN, and Donley et al. IR-AGN samples with matched stellar mass, sSFR, and redshift distributions. We use these as control samples to compare the clustering of galaxies that host AGNs to similar galaxies without AGNs. This limits the effect of AGN selection biases such as AGNs being

preferentially identified in galaxies with high stellar mass (e.g., Aird et al. 2012). Additionally, comparing the clustering of AGNs to matched galaxy samples cancels out any effective flux limits that arise from either the multi-wavelength AGN selection or the spectroscopic redshift requirement (e.g., Leauthaud et al. 2015). Effectively, we use individual matched galaxy control samples for each of the X-ray AGN, radio AGN, and Donley et al. IR-AGN samples to control for differences in the host galaxy properties that each AGN selection identifies. Coil et al. (2009) and Hickox et al. (2009) created similar matched galaxy samples; however, they matched rest-frame optical magnitude and color. While these are easily observed properties, they are not as physically motivated as stellar mass and sSFR. While we find no significant differences in our results matching joint stellar mass, sSFR, and redshift distributions rather than magnitude, color, and redshift distributions, we use the former parameters as they reflect intrinsic host galaxy physical properties.

We measure the joint stellar mass, sSFR, and redshift distribution for each of the X-ray AGN, radio AGN, and Donley et al. IR-AGN samples in stellar mass bins of $\Delta M_* = 0.2$ dex, sSFR bins of $\Delta \text{sSFR} = 0.2$ dex, and redshift bins of $\Delta z = 0.1$. The projected distributions of each sample are shown in Figure 6. Normalizing each distribution by the total number of galaxies in each bin results in the observed fraction of AGNs in that bin, effectively estimating the probability density in this three-dimensional parameter space. We use this as an estimate of the probability density to weight each inactive galaxy when creating matched galaxy samples to compare to various AGN samples. To ensure that we can robustly estimate the stellar masses and SFRs of the AGNs, we limit the comparison of matched galaxies to AGN that do not have any broadline emission in their optical spectra, such that the optical light is dominated by the host galaxy.

4. CLUSTERING ANALYSIS

We measure the spatial distribution of AGNs using the two-point correlation function, which quantifies the excess probability above Poisson of finding two sources with a given physical separation. While most studies measure the auto-correlation function (ACF) of the AGN sample of interest, here we measure the cross-correlation function (CCF) of AGNs with galaxies, from which we then infer the ACF of the AGN alone. As discussed in Coil et al. (2009), there are two main advantages to this method. First, the CCF of AGNs and galaxies has a much greater statistical power due to the larger number density of galaxies, which better probe the underlying dark matter distribution where AGNs are located. Second, it does not require a complete understanding of the AGN selection function, which may not be well understood. Instead, all that is required is an understanding of the selection function of the galaxy tracer sample.

4.1. Measuring the CCF

The two-point correlation function $\xi(r)$ is defined as the excess probability density, dP/dV , above that of a Poisson random field, of a second source being physically separated by a distance r from a given source

$$\frac{dP}{dV} = n[1 + \xi(r)], \quad (11)$$

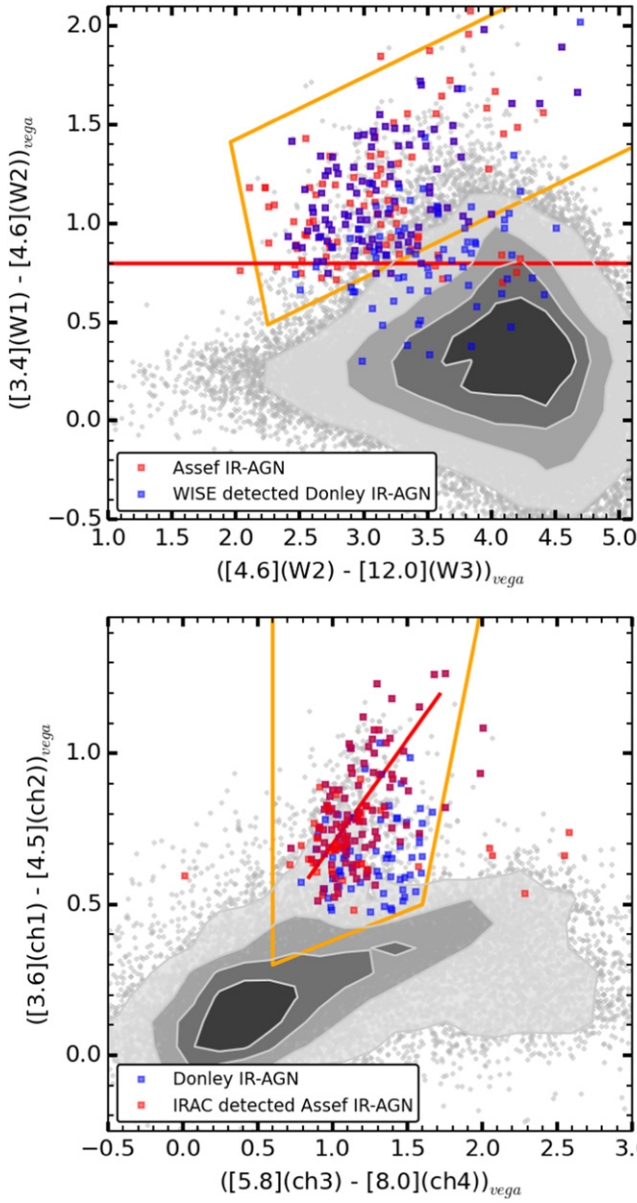


Figure 4. Comparison of the Donley et al. IR-AGN (blue) and Assef et al. IR-AGN (red) samples. Top: *WISE* color-color diagram with the Mateos et al. (2013) selection wedge shown in orange and the Stern et al. (2012) color selection shown in red. *WISE* sources identified by the Assef et al. IR-AGN selection technique are shown with red points and Donley et al. IR-AGN that are also detected in *WISE* are shown with blue points. Gray contours show all PRIMUS galaxies that are detected in *WISE*. Bottom: IRAC color-color diagram with the Stern et al. (2005) selection wedge shown in orange and the power-law locus indicated in red. Assef et al. IR-AGNs are shown with red points and Donley et al. IR-AGNs are shown with blue points. A small number of the Assef et al. IR-AGNs that are IRAC-detected fall outside of the power-law region and Stern wedge, due to the selection not utilizing the longer *WISE* wavelengths.

where n is the mean number density of the sample of interest (Peebles 1980). The ACF measures the clustering of a single sample, where the two sources are from the same sample, while the CCF measures the clustering of one type of source, taken from one sample, around that of another type of source, taken from a second sample. Here we measure the CCF of AGNs (A) around galaxies (G), which are used as a tracer sample, and find the excess probability above random (R) of finding AGNs and

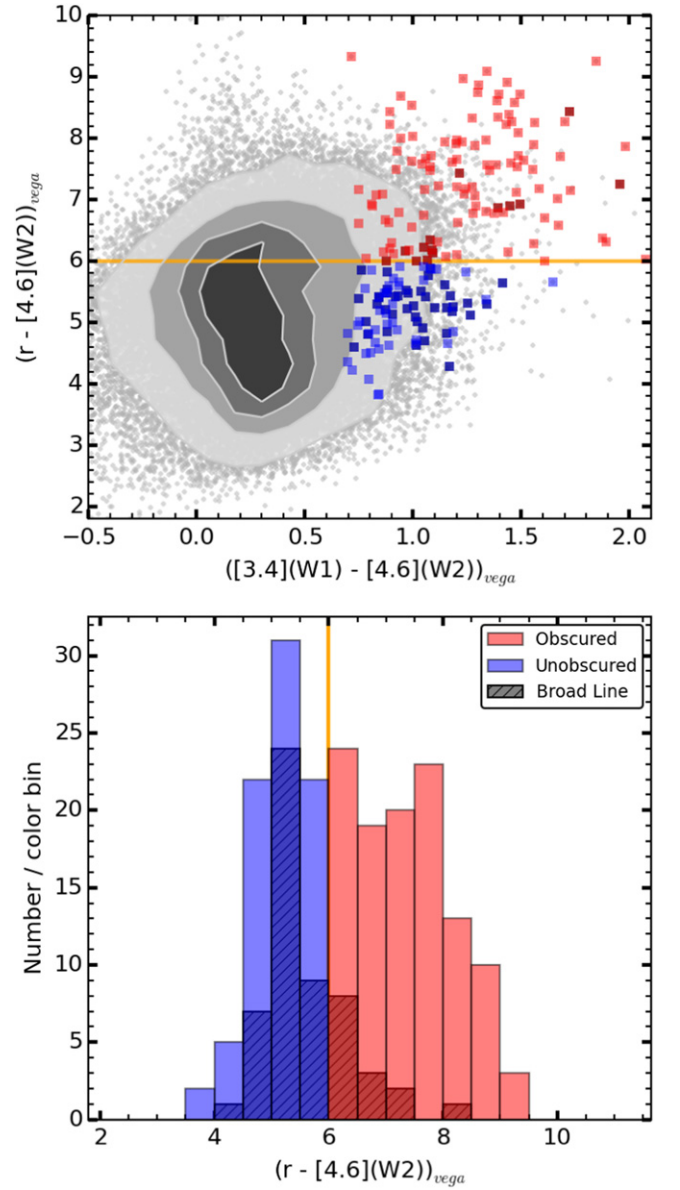


Figure 5. Comparison of obscured and unobscured Assef et al. IR-AGNs. Top: Yan et al. (2013) optical and MIR color selection plot showing obscured (red) and unobscured (blue) Assef et al. IR-AGNs. *WISE*-detected PRIMUS galaxies are shown with gray contours. Bottom: optical-to-MIR color distribution for Assef et al. IR-AGNs. Obscured Assef et al. IR-AGNs are shown with a red histogram, unobscured Assef et al. IR-AGNs with a blue histogram, and the broadline Assef et al. IR-AGNs with a black histogram. Most broadline sources have optical-to-MIR colors of unobscured AGNs.

galaxies with a given separation (r). We use the Davis & Peebles (1983) estimator:

$$\xi(r) = \frac{AG(r)}{AR(r)} - 1, \quad (12)$$

where $AG(r)$ is the sum of the weighted AGN-galaxy pairs and $AR(r)$ is the sum of the weighted AGN-random pairs, both as a function of separation. Weights are used to account for target selection in the PRIMUS sample (see Section 2.4); by applying these weights, we are able to create a statistically complete sample that is not subject to spatial biases. In the DEEP2 fields, the weights are included in the spatial selection function which

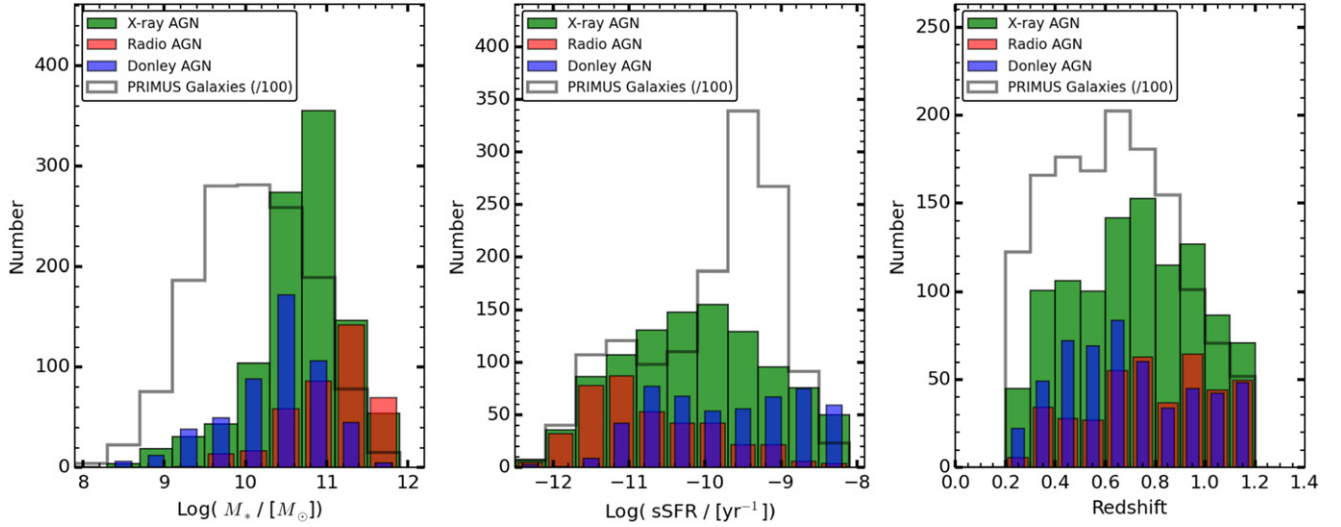


Figure 6. Stellar mass, sSFR, and redshift distributions for the X-ray AGN, radio AGN, Donley et al. IR-AGN, and galaxy tracer samples. The green, red, and blue filled histograms show the distributions of the X-ray AGNs, radio AGNs, and Donley et al. IR-AGNs, respectively. The gray line showing the distributions for the galaxy tracer sample is scaled down by a factor of 100 for ease of comparison. Differences between the underlying galaxy sample and AGNs identified at different wavelengths are dominated by the difficulty in selecting AGNs of a given specific accretion rate in low-mass galaxies (e.g., Aird et al. 2012). Additionally, there are substantial differences in the stellar mass, sSFR, and redshift distributions between AGNs identified at different wavelengths.

we use to generate the random catalogs, such that galaxies have unity weight. We calculate the weighted number of pairs:

$$AG = \sum_{\substack{i \in A \\ j \in G}} \frac{w_{\text{AGN};i} \times w_{\text{galaxy};j}}{W_{\text{AGN}} \times W_{\text{galaxy}}} \quad (13)$$

$$AR = \sum_{i \in A} \frac{w_{\text{AGN};i}}{W_{\text{AGN}} \times N_{\text{random}}}, \quad (14)$$

where w_{AGN} is the weight of a given AGN, w_{galaxy} is the weight of a given galaxy, W_{AGN} is the total AGN weight, W_{galaxy} is the total galaxy weight, and N_{random} is the number of random objects. The AGN weight is the multiplicative combination of the targeting weight and any additional completeness weight such as the X-ray AGN weight (see Section 2.1 for details). For the DEEP2 fields, the targeting weight is unity for each source.

Peculiar velocities distort $\xi(r)$ measurements in the redshift direction along the line of sight. We therefore measure $\xi(r)$ in two dimensions, $\xi(r_p, \pi)$, where r_p is the separation perpendicular to the line of sight, which is unaffected by peculiar velocities, and π is the separation along the line of sight. Integrating $\xi(r_p, \pi)$ along the π dimension leads to a statistic that is independent of redshift space distortions, the projected correlation function:

$$w_p(r_p) = 2 \int_0^\infty d\pi \xi(r_p, \pi) \quad (15)$$

$$\approx 2 \int_0^{\pi_{\text{max}}} d\pi \xi(r_p, \pi), \quad (16)$$

where π_{max} is the maximum π separation to which we integrate. As the S/N of $\xi(r_p, \pi)$ declines quickly for large values of π , we measure the projected correlation function by integrating to a given π_{max} to limit shot noise. We use a larger π_{max} value in the PRIMUS fields compared to the DEEP2 fields to account for the larger redshift uncertainty in the PRIMUS survey. In the PRIMUS fields we use $\pi_{\text{max}} = 80 h^{-1}$ Mpc, while in DEEP2 we use $\pi_{\text{max}} = 20 h^{-1}$ Mpc. Skibba et al.

(2014) and Coil et al. (2008) use similar values for these surveys, respectively.

4.2. Jackknife Uncertainty Estimation

We estimate the uncertainty in our measurements using jackknife resampling of the data (e.g., Lupton 1993; Scranton et al. 2002). For reasonably large surveys (including both PRIMUS and DEEP2), jackknife errors are generally similar to the cosmic variance errors in w_p derived from simulated mock catalogs (e.g., Zehavi et al. 2005; Coil et al. 2008; Norberg et al. 2008; Skibba et al. 2014). For each of our samples, we use between 10 and 12 jackknife samples across our 8 fields, where we have spatially subdivided the larger fields into 2 or more subfields. The different number of jackknife samples is due to the multi-wavelength coverage in each field (i.e., CDFS does not contain X-ray data; see Table 1 for field details.) We subdivide the large fields (CDFS and XMM) along lines of constant R.A. and decl. such that the resulting subsamples probe roughly similar volumes and cover an area on the sky approximately equal to $\sim 1 \text{ deg}^2$.

The uncertainty in w_p is estimated by calculating the projected correlation function using each jackknife sample. From this collection of w_p estimates, we calculate the variance in the projected correlation function,

$$\sigma_{w_p}^2(r_p) = \frac{N-1}{N} \sum_j (w_p(r_p) - \hat{w}_j(r_p))^2, \quad (17)$$

where the N is the number of jackknife samples, j indexes each jackknife sample, and $\hat{w}_j(r_p)$ is the projected correlation function computed for a given jackknife sample. By measuring the projected correlation function using multiple fields across the sky, the jackknife resampling of fields estimates the uncertainty on our measurements due to cosmic variance.

4.3. Inferring the AGN Auto-correlation Function

Following Coil et al. (2009), we infer the AGN ACF from measurements of the AGN-galaxy CCF and the galaxy ACF. We calculate the galaxy ACF using the Landy & Szalay (1993) estimator:

$$\xi(r_p, \pi) = \frac{GG(r_p, \pi) - 2GR(r_p, \pi) + RR(r_p, \pi)}{RR(r_p, \pi)}, \quad (18)$$

where GG , GR , and RR are the galaxy–galaxy, galaxy–random, and random–random weighted pair counts, respectively, where we include the galaxy targeting weights. We calculate the AGN-galaxy CCF and galaxy ACF in the same volume. We integrate the galaxy ACF projected correlation function to the same π_{\max} limits used for the AGN-galaxy CCF.

We then infer the ACF of the AGN sample using

$$w_{AA}(r_p) = \frac{w_{AG}^2(r_p)}{w_{GG}(r_p)}, \quad (19)$$

where w_{AA} is the projected AGN ACF, w_{AG} is the projected AGN CCF, and w_{GG} is the projected galaxy ACF. Implicit is the assumption that the spatial distributions of AGNs and galaxies are linearly related to the underlying dark matter spatial distribution (i.e., that the bias is linear; see Section 4.5 below), and that galaxies and AGNs are well mixed within dark matter halos.

4.4. Power-law Fits

The correlation function can roughly be fit by a power law, with $\xi(r) = (r/r_0)^\gamma$, where the scale factor r_0 is the scale at which there is unity excess probability and $\xi = 1$. An analytic form can then be fit to $w_p(r_p)$:

$$w_p(r_p) = r_p \left(\frac{r_0}{r_p} \right)^\gamma \frac{\Gamma\left(\frac{1}{2}\right)\Gamma\left(\frac{\gamma-1}{2}\right)}{\Gamma\left(\frac{\gamma}{2}\right)}, \quad (20)$$

where Γ is the Gamma function. We fit this analytic function to our clustering measurements in the approximately linear regime of $r_p = 1 - 10 h^{-1}$ Mpc. On larger scales, the size of our fields limits the number of pair counts, which artificially lowers the measured correlation function and leads to large statistical fluctuations.

4.5. Bias Estimation

We use the projected correlation function to estimate the dark matter bias of the AGN ACF. The bias b measures the relative clustering strength of the AGN sample to that of dark matter particles. We estimate the bias at the median redshift of each AGN sample using the publicly available code of Smith et al. (2003). We integrate the dark matter correlation function to a $\pi_{\max} = 80 h^{-1}$ Mpc and then calculate the bias as

$$b = \sqrt{\frac{w_{\text{AGN}}}{w_{\text{DM}}}}, \quad (21)$$

where w_{AGN} is the AGN ACF and w_{DM} is the dark matter ACF on scales of $r_p = 1 - 10 h^{-1}$ Mpc. When comparing the clustering of different samples, it is useful to compare the bias values instead of the clustering scale lengths, as the bias

accounts for differences in the median redshift of each sample and further does not assume that ξ is a power law.

Additionally, the relative bias between two AGN or galaxy samples is defined as the square root of the ratio of their respective projected correlation functions. This allows for a simple comparison of the clustering strength of two samples and is akin to comparing their absolute bias (relative to dark matter) values. We estimate the relative bias on scales of $r_p = 1 - 10 h^{-1}$ Mpc. We use the ratio of CCFs which does not increase the fractional uncertainty of the resulting bias due to the common galaxy tracer ACF term in the AGN ACF. Below we present the mean and 1σ uncertainty of the relative bias across the jackknife samples when comparing two samples.

4.6. Halo Mass Estimation

We estimate the median dark matter halo mass (M_{DM}) that hosts AGNs selected at different wavelengths from the absolute bias measured on scales of $r_p = 1 - 10 h^{-1}$ Mpc. We convert the bias to the quantity $\nu = \delta_c/\sigma(M)$, where $\delta_c \sim 1.69$ is the critical density for collapse and $\sigma(M)$ is the mass density fluctuation in a sphere of radius $r^3 = (3M\Delta/4\pi\bar{\rho})$ from linear theory. We use Equation (8) of Sheth et al. (2001) to convert the absolute bias to ν and Equations (A8)–(A10) of van den Bosch (2002) to infer the median M_{DM} of the sample.

5. RESULTS

In this section, we present the results of our correlation function analysis. As discussed above, we measure the CCF of our AGN samples relative to the galaxy tracer sample and the ACF of the galaxy tracer sample, in order to infer the ACF of the various AGN samples. We first present the ACF of the X-ray AGNs, radio AGNs, and Donley et al. IR-AGNs in Section 5.1. We then compare the clustering properties of various subsamples within each of the X-ray AGN, radio AGN, and Donley et al. IR-AGN samples in Section 5.2 to investigate whether the clustering amplitude depends on AGN luminosity or hardness ratio. In Section 5.3 we present the clustering of obscured versus unobscured IR-AGNs selected in *WISE*. We compare the relative clustering between X-ray AGNs, radio AGNs, and Donley et al. IR-AGNs in Section 5.4 to determine whether AGNs selected at different wavelengths have different clustering amplitudes. Finally, we compare the clustering strength of each AGN sample relative to matched galaxy control samples in Section 5.6.

5.1. Clustering of X-Ray, Radio, and IR-AGNs

In the left panel of Figure 7 we show the X-ray AGN ACF (black), which is derived from the AGN-galaxy CCF (red) and the galaxy tracer ACF (blue). In this figure, we present results including (gray) and excluding (black) the COSMOS field. The X-ray AGN ACF is more clustered than the galaxy tracer sample. Table 3 lists the measured r_0 and γ values excluding the COSMOS field, as well as the absolute bias and inferred median dark matter halo mass both with and without the COSMOS field included. As can be seen in Figure 7, the clustering amplitude of X-ray AGNs increases when the COSMOS field is included; the bias on large scales increases by 26%. As discussed above, the COSMOS field contains several large structures at $z < 1$, which both systematically increases the clustering amplitude when including this field and

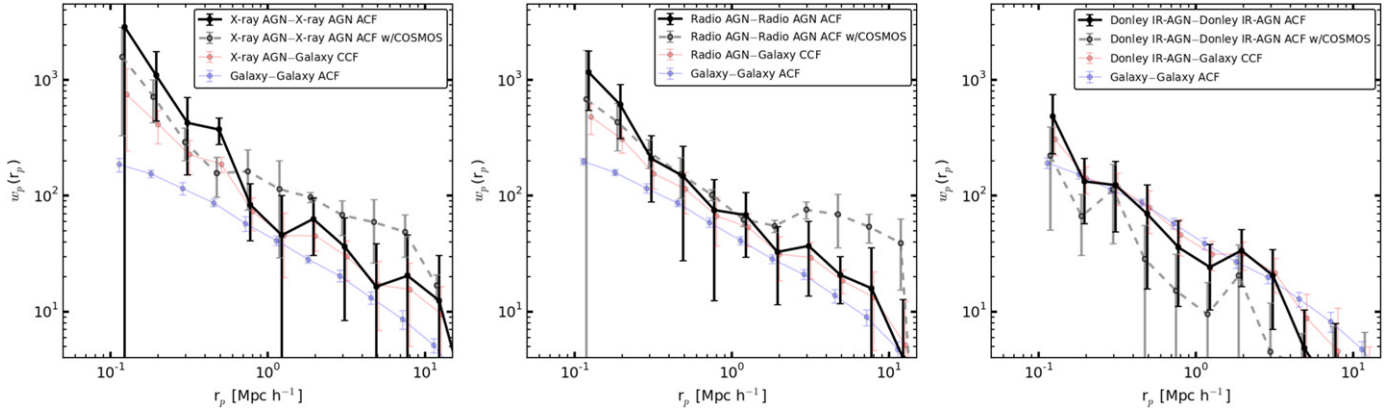


Figure 7. Projected correlation functions for the X-ray AGN (left), radio AGN (center), and Donley et al. IR-AGN (right) samples. In each panel, we show the AGN auto-correlation function (ACF; black), the galaxy-AGN cross-correlation function (CCF; red), and the galaxy tracer ACF (blue), as well as the uncertainties from jackknife resampling of the fields. The black line shows our fiducial sample which excludes the COSMOS field, while the light gray dashed line shows the ACF including the COSMOS field. As discussed in Section 2, the large overdensities in the COSMOS field at $z < 1$ can systematically affect the measured clustering amplitudes, as seen here.

Table 3
Clustering Results for X-Ray, Radio, and IR-AGNs

AGN Selection	Sample Name	r_0^a	γ^b		$\langle M_{\text{DM}} \rangle^d$	Bias ^c	
			Without the COSMOS Field			With the COSMOS Field	
X-ray AGNs	Fiducial	4.0 ± 1.9	1.5 ± 0.2	1.5 ± 0.2	12.9	1.9 ± 0.1	13.3
Radio AGNs	Fiducial	5.5 ± 1.9	1.9 ± 0.7	1.8 ± 0.1	13.3	2.7 ± 0.7	13.8
Donley IR-AGNs	Fiducial	4.8 ± 1.3	1.9 ± 0.3	1.3 ± 0.5	12.8	0.9 ± 0.2	11.6
X-ray AGNs	Non-broadline	7.0 ± 6.0	1.4 ± 0.3	2.5 ± 0.4	13.6	1.9 ± 0.2	13.4
Radio AGNs	Non-broadline	5.7 ± 2.8	1.6 ± 0.6	1.9 ± 0.3	13.3	2.6 ± 0.7	13.8
Donley IR-AGNs	Non-broadline	4.9 ± 1.5	1.7 ± 0.3	1.4 ± 0.5	12.9	1.1 ± 0.3	12.5
X-ray AGNs	Low L_X	4.5 ± 4.3	1.3 ± 0.3	1.9 ± 0.3	13.3	2.0 ± 0.2	13.4
X-ray AGNs	High L_X	4.1 ± 1.8	1.6 ± 0.4	1.5 ± 0.1	12.9	1.8 ± 0.2	13.2
X-ray AGNs	Low λ	6.0 ± 3.6	1.6 ± 0.4	2.0 ± 0.2	13.3	2.1 ± 0.2	13.5
X-ray AGNs	High λ	3.8 ± 1.0	1.5 ± 0.3	1.4 ± 0.2	12.9	1.8 ± 0.3	13.3
X-ray AGNs	Low HR	3.2 ± 1.6	1.4 ± 0.3	1.4 ± 0.2	12.8	2.0 ± 0.0	13.4
X-ray AGNs	High HR	5.0 ± 2.1	1.7 ± 0.7	1.6 ± 0.2	13.1	1.6 ± 0.4	13.1
X-ray AGNs	Low Redshift	2.7 ± 1.8	1.6 ± 0.4	0.9 ± 0.2	12.0	1.6 ± 0.2	13.4
X-ray AGNs	High Redshift	6.1 ± 2.1	2.3 ± 0.7	2.0 ± 0.5	13.3	2.7 ± 0.6	13.6
Radio AGNs	High $P_{1.4 \text{ GHz}}$	5.7 ± 2.0	2.3 ± 1.0	1.9 ± 0.3	13.3	2.2 ± 0.6	13.6
Radio AGNs	Low $P_{1.4 \text{ GHz}}$	4.3 ± 5.0	1.4 ± 1.2	1.7 ± 0.3	13.2	2.9 ± 0.7	13.9
Assef IR-AGNs	Fiducial	2.3 ± 1.3	1.8 ± 1.0	0.8 ± 0.1	11.2	0.8 ± 0.1	11.4
Assef IR-AGNs	Obscured <i>WISE</i> color	0.8 ± 1.6	1.3 ± 0.5	0.7 ± 0.2	11.1	0.6 ± 0.2	11.1
Assef IR-AGNs	Unobscured <i>WISE</i> color	2.7 ± 0.9	3.1 ± 3.8	0.9 ± 0.2	11.7	1.1 ± 0.3	12.4

Notes.

^a Correlation scale length, r_0 , in units of [h^{-1} Mpc].

^b Correlation power-law index γ .

^c Absolute bias estimated on scales of $1 < r_p / [h^{-1} \text{ Mpc}] \leq 10$.

^d Dark matter halo median mass, M_{DM} , in units of [$\log(h^{-1} \mathcal{M}_{\odot})$].

increases the jackknife error. We therefore prefer to focus on results that exclude COSMOS when discussing the absolute bias of our AGN samples. The bias of X-ray AGNs that we measure ($b = 1.5 \pm 0.2$) corresponds to a median dark matter halo mass of $\langle M_{\text{halo}} \rangle \sim 10^{12.9} h^{-1} \mathcal{M}_{\odot}$, which is generally associated with galaxy groups. The X-ray AGN ACF rises sharply at small projected separations ($r_p < 0.7 h^{-1}$ Mpc), indicating that on small scales there is an increase in the number of pairs of objects within the same dark matter halo.

In the center panel of Figure 7, we show the radio AGN ACF, again with (gray) and without (black) the COSMOS field

included. Including COSMOS causes the large-scale bias to increase substantially by 50%. We find that similar to X-ray AGNs, radio AGNs are more clustered than the galaxy tracer sample and have a large bias value ($b = 1.8 \pm 0.1$, excluding COSMOS), which suggest that they reside in massive dark matter halos ($\langle M_{\text{halo}} \rangle \sim 10^{13.3} h^{-1} \mathcal{M}_{\odot}$) typically associated with massive groups or small clusters.

In the right panel of Figure 7, we show the Donley et al. IR-AGN ACF. Unlike the X-ray AGNs and radio AGNs, we find that Donley et al. IR-AGNs are *less* clustered than the galaxy tracer sample. The Donley et al. IR-AGN sample has a lower

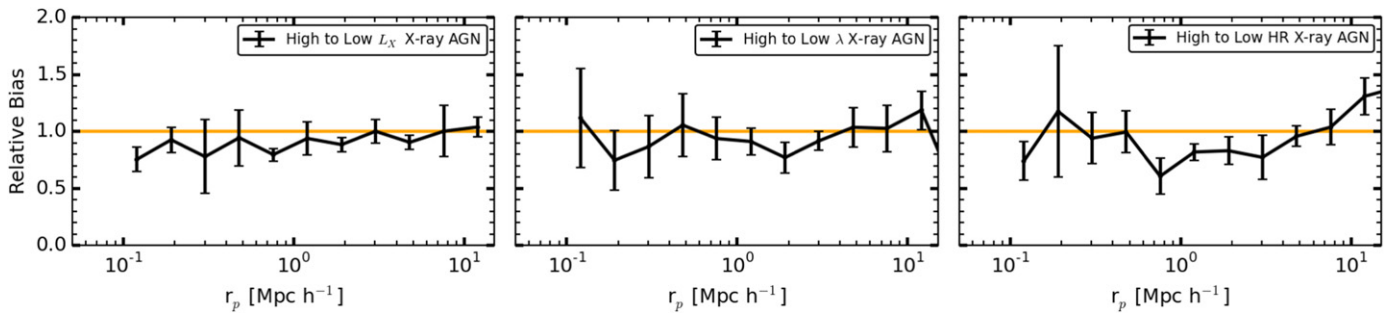


Figure 8. Scale-dependent relative bias between various X-ray AGN samples defined by X-ray luminosity (L_X , left), specific accretion rate (λ , center), and hardness ratio (HR, right). Error bars are derived using jackknife resampling of the fields.

bias value ($b = 1.3 \pm 0.5$, excluding COSMOS) than either of the X-ray AGNs or radio AGNs, from which we estimate a median dark matter halo mass of ($\langle M_{\text{halo}} \rangle \sim 10^{12.8} h^{-1} M_{\odot}$). Unlike for the X-ray AGN and radio AGN samples, including COSMOS for Donley et al. IR-AGN sample results in a lower clustering amplitude; the bias decreases by 30%.

While not shown here, we additionally measure the Assef et al. IR-AGN ACF and list the derived clustering parameters in Table 3. Similar to the Donley et al. IR-AGN sample, the Assef et al. IR-AGN sample is less clustered than the galaxy tracer sample and has a lower bias ($b = 0.8 \pm 0.1$) than either the X-ray AGNs or radio AGNs. The large-scale bias of the Assef et al. IR-AGN sample does not change when including the COSMOS field, though there is an increase in the clustering strength on small scales which substantially increases the slope ($\gamma = 2.2$). We also measured the clustering properties of Assef et al. IR-AGNs and find similar results to both Donley et al. IR-AGNs and Assef et al. IR-AGNs.

5.2. Relative Bias within AGN Samples at a Given Wavelength

As discussed above, the COSMOS field contains large overdensities at $z \sim 0.3$ and $z \sim 0.7$ (e.g., McCracken et al. 2007; Lilly et al. 2007; Meneux et al. 2009; de la Torre et al. 2010; Kovač et al. 2010; Skibba et al. 2014). In our sample, which combines the PRIMUS and DEEP2 fields and therefore covers a large volume and probes a range of cosmic densities, we find including the COSMOS field systematically impacts our clustering results (somewhat akin to the Sloan Great Wall; e.g., Zehavi et al. 2011; McBride et al. 2011), both in terms of the measured amplitude and the jackknife errors, which increase when COSMOS is included.

However, including the COSMOS field is more robust when comparing the *relative* bias between two samples, as the same volume is used for both measurements and overall changes in the density (i.e., cosmic variance) cancel to first order. This is reflected in the fact that the fractional jackknife errors on the relative bias values measured here *decrease* when the COSMOS field is included (which results in larger samples and volumes probed). Therefore, when presenting relative bias measurements throughout the paper, we include the COSMOS field. We note that if the COSMOS field is excluded from our relative bias analysis, the significance of our results lowers (due to the larger errors) but the actual relative bias values do not change substantially.

As discussed in Section 3, we divide the full X-ray AGN sample into subsamples depending on various AGN properties: X-ray luminosity L_X , specific accretion rate λ , and hardness

ratio. The measured clustering parameters for each subsample are given in Table 3. The relative bias between these samples is shown in Figure 8 and listed in Table 4 for scales associated with the one-halo term ($r_p < 1 h^{-1} \text{Mpc}$) and the two-halo term ($r_p > 1 h^{-1} \text{Mpc}$). As above, uncertainties are derived from jackknife resampling of the fields, and COSMOS is included here. We find a 2.6σ difference on small scales with L_X , such that the lower L_X sources are more clustered in the one-halo regime. For these X-ray samples defined by L_X , λ , and hardness ratio we find no statistically significant differences ($>3\sigma$) in the clustering amplitudes on either small or larger scales. This implies that the mass of dark matter host halo does not correlate with any of these properties within the ranges that we probe.

In the left panel of Figure 9, we show the relative bias between high- and low-luminosity radio AGNs. We do not find significant differences in the clustering of high- and low-luminosity radio AGNs on either small or large scales (see Table 4). The lack of a dependence of the clustering amplitude on radio luminosity may be surprising, given that the highest luminosity radio AGNs are found in the most massive quiescent galaxies compared to lower luminosity radio AGNs (bottom panel of Figure 3). While the lower luminosity radio AGN sample contains more galaxies with slightly lower mass ($\mathcal{M}_{*} \sim 10^{10.8} M_{\odot}$, compared to $\mathcal{M}_{*} \sim 10^{11.2} M_{\odot}$ for the high-luminosity sample), the clustering signal is dominated by the most massive objects in the sample. Additionally, we find no significant difference in the sSFR distribution of the host galaxies as a function of the radio luminosity, which suggests that high- and low-luminosity radio AGNs have fairly similar host galaxies.

For each of the AGN properties tested above (i.e., luminosity, specific accretion rate), we test the significance of the clustering differences when comparing sources in the upper and lower quartiles, as opposed to the upper and lower halves. This allows us to look for clustering differences between the most extreme sources in each parameter of interest. This does not change any of our results; however, the larger uncertainties that result from using smaller samples may prevent us from detecting any underlying differences.

In the center panel of Figure 9, we show the relative bias between the Donley et al. IR-AGN and Assef et al. IR-AGN samples. We list the measured clustering parameters in Table 3 and relative bias between these samples in Table 4. We find that these samples have consistent clustering properties, given the error bars; however, the bias of Donley et al. IR-AGNs is 37% higher than that of the

Table 4
Relative Clustering Bias for X-Ray, Radio, and IR-AGN Samples, Including the COSMOS Field

AGN Sample Comparison	Relative Bias $0.1 < r_p < 1$	N_σ	Relative Bias $1 < r_p < 10$	N_σ
Full X-ray AGN to Full Radio AGN ratio	0.96 ± 0.04	-1.0	0.87 ± 0.10	-1.3
Full X-ray AGN to Full Donley IR-AGN ratio	1.42 ± 0.10	4.4	1.53 ± 0.22	2.4
Full Radio AGN to Full Donley IR-AGN ratio	1.49 ± 0.16	3.0	1.81 ± 0.49	1.7
Full Assef IR-AGN to Full Donley IR-AGN ratio	1.41 ± 0.24	1.7	1.00 ± 0.19	0.0
No Broadline X-ray AGN to Full X-ray AGN ratio	0.95 ± 0.05	-1.0	1.01 ± 0.02	0.6
No Broadline Radio AGN to Full Radio AGN ratio	0.97 ± 0.04	-0.8	0.97 ± 0.03	-1.0
No Broadline Donley IR-AGN to Full Donley IR-AGN ratio	1.15 ± 0.09	1.6	1.16 ± 0.07	2.2
No Broadline X-ray AGN to No Broadline Radio AGN ratio	0.94 ± 0.09	-0.7	0.91 ± 0.08	-1.2
No Broadline X-ray AGN to No Broadline Donley IR-AGN ratio	1.17 ± 0.11	1.6	1.36 ± 0.18	2.0
No Broadline Radio AGN to No Broadline Donley IR-AGN ratio	1.25 ± 0.20	1.3	1.56 ± 0.51	1.1
High L_X to Low L_X X-ray AGN ratio	0.84 ± 0.06	-2.6	0.95 ± 0.05	-1.0
High λ to Low λ X-ray AGN ratio	0.95 ± 0.18	-0.3	0.93 ± 0.09	-0.7
High HR to Low HR X-ray AGN ratio	0.89 ± 0.15	-0.7	0.88 ± 0.09	-1.3
High $P_{1.4 \text{ GHz}}$ to Low $P_{1.4 \text{ GHz}}$ Radio AGN ratio	1.20 ± 0.15	1.4	0.87 ± 0.11	-1.2
Obscured to Unobscured Assef IR-AGN ratio	0.75 ± 0.12	-2.1	0.78 ± 0.27	-0.8
Low λ X-ray AGN to No Broadline Radio AGN ratio	1.00 ± 0.16	0.0	0.95 ± 0.08	-0.7
High λ X-ray AGN to No Broadline Donley IR-AGN ratio	1.18 ± 0.13	1.4	1.33 ± 0.26	1.3
No Broadline X-ray AGN to Matched Galaxy ratio	0.93 ± 0.12	-0.6	0.96 ± 0.05	-0.8
No Broadline Radio AGN to Matched Galaxy ratio	0.91 ± 0.17	-0.5	1.09 ± 0.07	1.3
No Broadline Donley IR-AGN to Matched Galaxy ratio	0.89 ± 0.08	-1.5	0.80 ± 0.16	-1.3

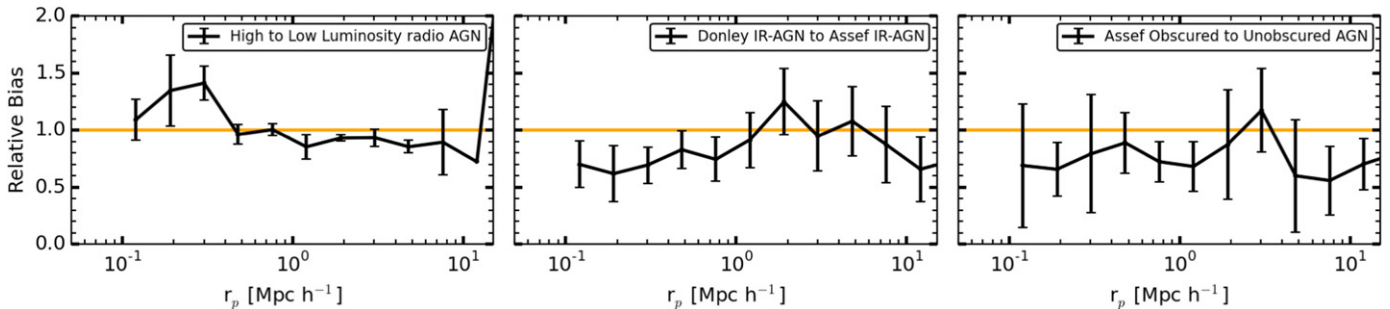


Figure 9. Relative bias between the high- and low-luminosity radio AGN samples (left), the Donley et al. IR-AGN and Assef et al. IR-AGN samples (center), and the obscured Assef et al. IR-AGN and unobscured Assef et al. IR-AGN (right). There is no significant difference between the clustering of these samples; all relative biases are consistent with unity.

Assef et al. IR-AGNs. Both samples have lower estimates for the median dark matter halo mass than the X-ray AGNs or radio AGNs.

5.3. Relative Bias of Obscured versus Unobscured *WISE* IR-AGNs

Following Donoso et al. (2014) and DiPompeo et al. (2014), we compare the clustering of obscured and unobscured *WISE*-selected AGNs. In the right panel of Figure 9, we show the scale-dependent relative bias between obscured and unobscured Assef et al. IR-AGNs. The obscured Assef et al. IR-AGNs are less clustered than the unobscured Assef et al. IR-AGNs at the $\sim 2\sigma$ level on small scales and at the $\sim 1\sigma$ level on larger scales. Within the uncertainties, therefore, we do not find a significant difference in the clustering amplitudes of these samples. This suggests that the differences found by Donoso

et al. (2014), where the COSMOS field alone was used to determine the redshift distributions of these two populations, was impacted by using a single field. Here, using eight fields that cover $\sim 9.1 \text{ deg}^2$ of the sky, and using spectroscopic redshifts for each source, we do not find a significant difference in their clustering.

To understand this further, we show in Figure 10 the redshift distributions of the obscured (red), unobscured (blue), and broadline Assef et al. IR-AGNs (black) in our sample. While the median redshift of the obscured Assef et al. IR-AGNs ($\langle z \rangle \sim 0.77$) and unobscured Assef et al. IR-AGNs ($\langle z \rangle \sim 0.70$) are similar, the samples have very different redshift distributions. The obscured AGNs peak at $\langle z \rangle \sim 0.7$, whereas the unobscured AGNs have a flatter distribution and peak at both lower and higher redshift at $\langle z \rangle \sim 0.3$ and $\langle z \rangle \sim 1.0$. Within the unobscured sample, the broadline

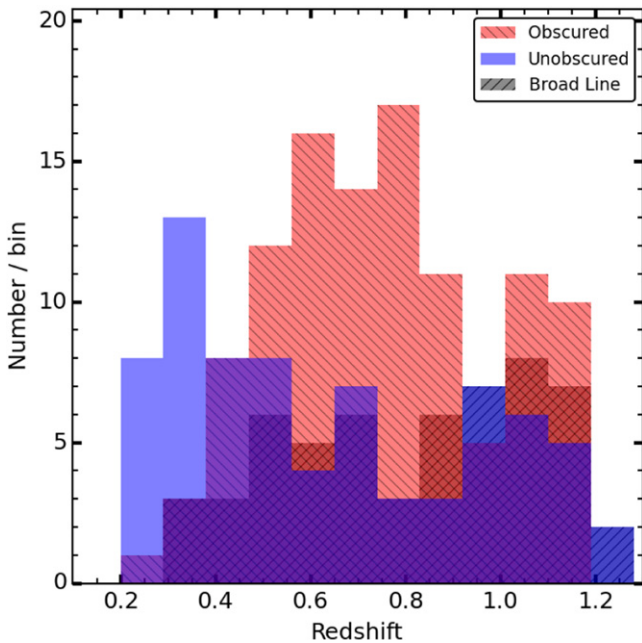


Figure 10. Redshift distributions for the obscured (red hatched), unobscured (blue), and broadline (dark gray hatched) Assef et al. IR-AGN. The obscured and unobscured IR-AGN populations have substantially different redshift distributions; the obscured sample peaks at $z \sim 0.7$, while the unobscured sample has a much flatter distribution, including more sources that are low redshift. The higher redshift sources in both samples are more likely to have broad optical lines.

sources typically have higher redshifts than the non-broadline sources.

The differences in the redshift distributions of obscured and unobscured Assef et al. IR-AGNs strongly limits the interpretation of angular clustering measurements of these two populations. While there are broad similarities between our redshift distribution and that of Donoso et al. (2014), our obscured sample shows a much broader redshift distribution extending out to $\langle z \rangle \sim 1.2$. Our unobscured sample also has a larger fraction of sources at low redshift ($\langle z \rangle \sim 0.3$). Our redshift distribution is more similar to the redshift distributions found in the Boötes Survey (DiPompeo et al. 2014).

Similarly, we test both the Donley et al. IR-AGN sample and Assef et al. IR-AGN samples for any dependence of the clustering amplitude with obscuration and find no significant differences. For Donley et al. IR-AGNs, we test both an optical-to-*WISE* color cut ($r - W2 = 6.0$) and an optical-to-IRAC color cut ($r - [4.6] = 6.1$) and find no significant differences using either cut.

5.4. Comparison of the Clustering of X-Ray, Radio, and IR-AGNs

In Figure 11 we show the relative bias between AGNs identified at different wavelengths; the results are given in Table 4. We find that radio AGNs are more clustered than X-ray AGNs (red line) on large scales (15% higher bias), but the difference is not significant (1.3σ). Comparing the X-ray AGN and Donley et al. IR-AGN samples (purple line), there is a significant difference (4.4σ) on small scales, where X-ray AGNs have a 38% higher bias, while on large scales X-ray AGNs having a 44% higher bias (2.4σ). Comparing the radio AGN and Donley et al. IR-AGN samples (cyan line), radio

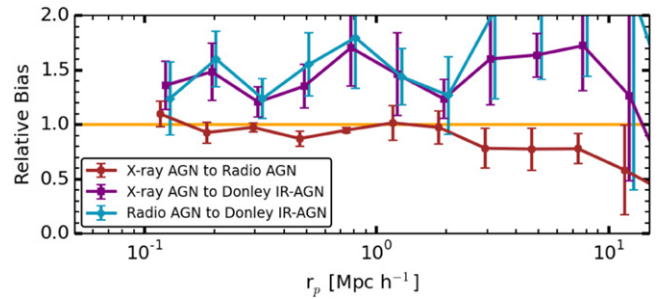


Figure 11. Relative bias between the X-ray, radio, and Donley et al. IR-AGN samples with error bars determined from jackknife resampling of the fields. We show the relative bias between X-ray to radio AGNs (dark red), X-ray to Donley et al. IR-AGNs (purple), and radio to Donley et al. IR-AGNs (cyan). We find that the X-ray and radio AGNs have similar clustering amplitudes, both of which are larger than that of Donley et al. IR-AGNs.

AGNs have a 40% higher bias on small scales (3.0σ) and an 58% higher bias on large scales (1.7σ). The relative bias averaged over all scales results in a difference at the 2.5σ level.

On small scales ($r_p < 1 h^{-1}$ Mpc), the correlation functions of both the X-ray AGNs and radio AGNs are significantly higher than that of the Donley et al. IR-AGNs. This may be due in part to the difficulty in identifying Donley et al. IR-AGNs in quiescent galaxies, due to the $1.4 \mu\text{m}$ stellar bump entering into the mid-IR photometry (Mendez et al. 2013). This selection effect limits the number of Donley et al. IR-AGNs that can be identified in quiescent host galaxies, which would decrease the clustering amplitude on all scales, though particularly on small scales (reflecting differences in color-dependent clustering; e.g., Zehavi et al. 2005; Coil et al. 2009; Skibba et al. 2014).

5.5. Dependence on Specific Accretion Rate

As shown in Hickox et al. (2009) and Mendez et al. (2013), there is a substantial difference in the specific accretion rate (λ) distributions of AGNs selected at different wavelengths. To account for these differences in λ , here we compare radio AGNs and Donley et al. IR-AGN to X-ray AGNs with similar λ values. In the large left panel of Figure 12, we show λ versus stellar mass for X-ray AGNs (green circles). X-ray AGNs that are also radio AGNs are shown with red diamonds, and those that are also Donley et al. IR-AGNs are shown with blue squares. We divide X-ray AGNs into a high- λ sample and a low- λ sample at $\lambda = 10^{-2} \text{ erg s}^{-1} \mathcal{M}_{\odot}^{-1}$. Most Donley et al. IR-AGNs lie above this line, while most radio AGNs lie below this line. Here we do not include sources below $\mathcal{M}_{*} \sim 10^{9.75} \mathcal{M}_{\odot}$ to ensure that we are roughly complete in stellar mass at all redshifts. We also remove all broadline sources from this comparison, as we require a stellar mass estimate for the high- λ X-ray AGN and low- λ X-ray AGN samples.

In the upper right panel of Figure 12, we show the scale-dependent relative bias between the high- λ X-ray AGNs and Donley et al. IR-AGNs. In the lower right panel of Figure 12, we show the relative bias between the low- λ X-ray AGNs (green) and radio AGNs (red). We find no significant differences between either sample. The limited significance of these results are dominated by the low number of non-broadline AGNs in each sample.

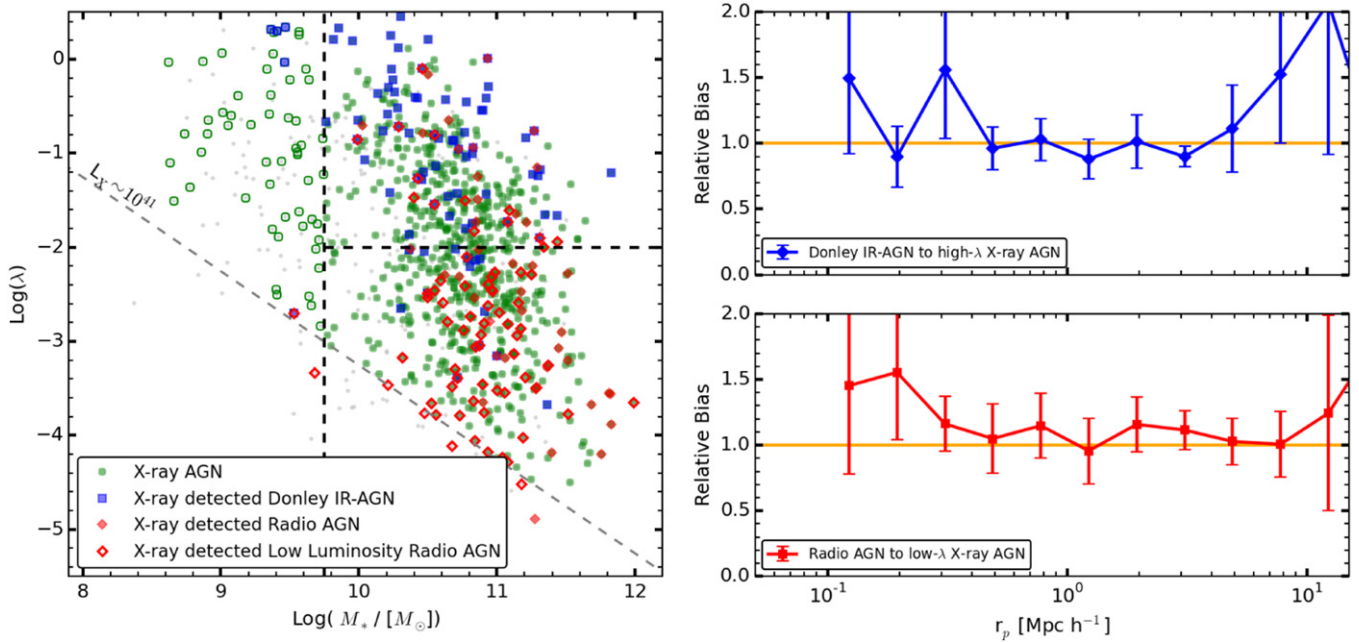


Figure 12. Dependence of clustering amplitude on specific accretion rate (λ) for X-ray, radio, and Donley et al. IR-AGNs. Left panel: specific accretion rate vs. stellar mass for X-ray-detected AGNs. X-ray AGNs that are also radio AGNs are shown with red diamonds, and those that are also Donley et al. IR-AGNs are shown with blue squares. The X-ray luminosity limit for our sample is shown as a light gray dashed diagonal line. X-ray AGNs below the $M_* = 10^{9.75} M_\odot$ stellar mass limit (vertical dashed line) are shown with open symbols, while X-ray AGNs with broad lines in their optical spectra are shown as small gray points. The $\lambda = -2$ line defines the high- λ and low- λ X-ray AGNs. Top right panel: relative bias between the high- λ X-ray AGNs and Donley et al. IR-AGNs for the non-broadline samples. Bottom right panel: relative bias between the low- λ X-ray AGNs and radio AGNs for the non-broadline samples. We find that Donley et al. IR-AGNs are similarly clustered as high- λ X-ray AGNs while radio AGNs are clustered similarly as low- λ X-ray AGNs.

5.6. Comparison with Matched Galaxy Control Samples

As discussed above, AGN samples identified at different wavelengths are biased in terms of identifying specific types of AGNs in specific types of host galaxies. In general, AGNs are more easily identified in more massive galaxies (e.g., Silverman et al. 2011; Aird et al. 2012). Additionally, there can be substantial differences in the sSFR and redshift distributions of the host galaxies of AGNs selected at X-ray, radio, and IR wavelengths (e.g., Coil et al. 2009; Hickox et al. 2009; Mendez et al. 2013; Goulding et al. 2014).

Differences in the host galaxy populations can influence the observed AGN clustering amplitude, which must be understood before AGN clustering can be used to constrain the AGN triggering mechanism. To account for this, we compare the clustering of each of our AGN samples to that of matched galaxy control samples that have the same stellar mass, sSFR, and redshift distributions as the AGN samples.

As this requires robust estimates of the stellar masses and SFRs, we remove optical BLAGNs for these comparisons in order to limit AGN contamination of the optical broadband photometry used in the SED fits. While broadline AGNs are a substantial fraction (34%) of the X-ray AGN population, excluding them does not significantly change the measured clustering properties. As seen in Table 3, excluding broadline AGNs from the fiducial X-ray AGN sample leads to a 1% change in the large-scale bias. This implies that at least for the L_X range and redshift range considered here, the clustering of narrow line and broadline X-ray AGNs are not significantly different. The radio AGN sample contains the smallest fraction of broadline sources (14%). Excluding the broadline radio sources results in only a 3% change in the bias on large scales. The broadline fraction of the Donley et al. IR-AGN sample is

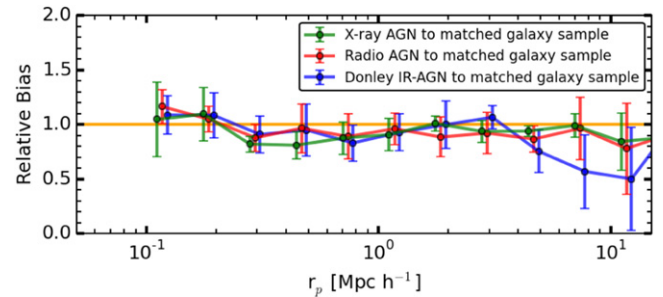


Figure 13. Relative bias between the X-ray AGNs (green), radio AGNs (red), and Donley et al. IR-AGNs (blue) and their respective stellar mass, sSFR, and redshift matched galaxy control samples. We do not find any significant differences in the clustering properties of any of the AGNs and matched galaxy samples; all relative biases are consistent with unity.

also substantial (31%), similar to that of the X-ray AGN sample, and excluding these sources leads to a 14% change in the bias. The relative biases *between* the X-ray, radio, and IR AGN samples after the broadline sources have been removed do not change too substantially, but the fractional errors do increase due to the smaller sample sizes.

In Figure 13 we show the relative biases between (non-broadline) AGN samples identified at different wavelengths and their matched control galaxy samples; the results are listed in Table 4. We find no significant differences in the clustering amplitude of either the X-ray AGNs, radio AGNs, or Donley et al. IR-AGNs and their matched galaxy control samples on small or large scales; all differences are significant at 1.5σ or less.

This suggests that the physical effect(s) of the host galaxy large-scale environment is either sub-dominant in AGN

triggering or is not separable from the host galaxy properties. The strong agreement between the clustering of AGN host galaxies and similarly selected inactive galaxies, on both small and large scales corresponding to the one- and two-halo terms, indicates that the AGN triggering mechanism either does not act on these scales or correlates with the properties of the galaxies in which they are identified. It could be possible, for example, that an environmental effect that triggers AGNs also causes changes in the host galaxy's sSFR, such that active and inactive galaxies with the same sSFR distribution have the same clustering properties. However, as shown elsewhere, there are not substantial correlations between host galaxy sSFR and AGN incidence once selection effects are taken into account (e.g., Aird et al. 2012; Azadi et al. 2015).

6. DISCUSSION

We have combined spectroscopic redshifts with multi-wavelength imaging to quantify the clustering properties of AGNs selected at different wavelengths and compared their clustering with matched galaxy samples. In this section, we discuss the implications of these findings. In Section 6.1 we compare our results to other multi-wavelength AGN clustering studies in the literature. In Section 5.5, we investigate whether AGN clustering amplitude depends on specific accretion rate, and in Section 6.2 we discuss the halo mass dependence of AGN activity.

6.1. Comparison with the Literature

In Figure 14 we compare the measured clustering amplitude of AGNs identified at different wavelengths using the bias parameter estimated on scales $1 h^{-1} \text{Mpc} < r_p < 10 h^{-1} \text{Mpc}$. We do not compare r_0 and γ values in the literature, due to the degeneracy between these parameters. In the top left panel, we compare the bias parameters for our three full samples selected at different wavelengths, while each of the other panels compares our results at a given wavelength with other results from the literature. In all panels the filled, colored symbols show our results excluding the COSMOS field, while the open, colored symbols include the COSMOS field.

In the top right panel, we compare the bias values of various X-ray AGN clustering studies. For each of the results shown that include the COSMOS field (our open symbol samples, Gilli et al. 2009; Allevato et al. 2011; Koutoulidis et al. 2013), the median dark matter halo mass of X-ray AGNs is above $\langle M_{\text{halo}} \rangle \sim 10^{13} h^{-1} \mathcal{M}_{\odot}$, while those that do not include the COSMOS field (Gilli et al. 2005; Yang et al. 2006; Coil et al. 2009; Hickox et al. 2009; Krumpe et al. 2010) find a median mass below $\langle M_{\text{halo}} \rangle \sim 10^{13.0} h^{-1} \mathcal{M}_{\odot}$. Both Gilli et al. (2005) and Yang et al. (2006) use one or two small fields ($< 0.5 \text{ deg}^2$) to measure the clustering of X-ray AGNs, which leads to an underestimate of the cosmic variance in their measurements. Including the COSMOS field systematically raises the bias due to the large overdensities found in the field at $z < 1$. Gilli et al. (2009) find an increase of $\sim 24\%$ in the bias when including the overdensity found at $z \sim 0.36$ within the COSMOS field. We find a similar $\sim 20\%$ increase. When we exclude COSMOS, we find similar results to Coil et al. (2009) and Hickox et al. (2009).

Interestingly, Allevato et al. (2011) and Koutoulidis et al. (2013) include the COSMOS field in their results and find X-ray AGN bias values similar to our fiducial results, which

exclude COSMOS. However, Allevato et al. (2011) derive their results using *only* the COSMOS field and bootstrap errors within that field, such that their errors due to cosmic variance are underestimated. The analysis in Koutoulidis et al. (2013) spans a very wide redshift range, $0 < z < 3$, and the results shown here are for the median redshift of their sample. This makes a direct comparison with results derived in smaller redshift bins somewhat difficult.

Taken together, all of these results show that X-ray AGNs are typically found in somewhat more massive dark matter halos at $\langle z \rangle \sim 0.9$ compared to $\langle z \rangle \sim 0.4$. The lower redshift X-ray AGNs have a lower median X-ray luminosity ($\langle L_X \rangle \sim 10^{42.3} \text{ erg s}^{-1}$) compared to the higher redshift X-ray AGN ($\langle L_X \rangle \sim 10^{43.2} \text{ erg s}^{-1}$). However, we do not find a correlation between clustering amplitude and X-ray luminosity in our samples, which suggests that the luminosity differences between the redshift samples is not driving the difference in clustering strength. We also do not find a significant difference in the median stellar mass of the lower redshift AGN hosts in our sample ($\langle M_{*} \rangle \sim 10^{10.7} \mathcal{M}_{\odot}$) compared to the higher redshift hosts ($\langle M_{*} \rangle \sim 10^{10.8} \mathcal{M}_{\odot}$). This difference is similar to that of the low X-ray luminosity AGN ($\langle M_{*} \rangle \sim 10^{10.7} \mathcal{M}_{\odot}$) and high X-ray luminosity AGN ($\langle M_{*} \rangle \sim 10^{10.8} \mathcal{M}_{\odot}$) samples, suggesting that differences in stellar mass are not driving the redshift-dependent results seen here.

In the bottom left panel, we show the bias of radio AGNs compared to results in the literature. Generally, the bias we measure agrees well with other published studies and indicates a relatively high dark matter halo mass of $\langle M_{\text{halo}} \rangle \sim 10^{13.3} h^{-1} \mathcal{M}_{\odot}$. Including the COSMOS field again increases the bias by $\sim 50\%$ but also substantially increases the error bars, due to one field having a systematically different clustering amplitude compared to the other fields. The Wake et al. (2008) results are higher than other measurements and are derived from the cross-correlation of radio-loud luminous red galaxies (LRGs; $P_{1.4 \text{ GHz}} > 10^{24} \text{ Watts Hz}^{-1}$) with the main 2SLAQ LRG survey. Their radio-detected LRGs have luminosities of $3\text{--}5L_{*}$, far higher than the average radio AGNs, which may account for their high bias value. Our low-luminosity radio AGNs have a consistent bias value as the Donoso et al. (2010) and Hickox et al. (2009) samples.

In the bottom right panel, we show the IR-AGNs selected using the Donley et al. IR-AGN selection technique (blue diamond) and the Assef et al. IR-AGN selection technique (red square). We additionally show the Assef et al. IR-AGN obscured (red diamond) and unobscured (red circle) subsamples. We compare our results to those of Hickox et al. (2009, gray diamond, $z \sim 0.5$) and Gilli et al. (2007, gray square, $z > 0.7$), as well as angular clustering estimates from Donoso et al. (2014) and DiPompeo et al. (2014) for obscured and unobscured sources. While the individual selection techniques compared (e.g., Donley et al. IR-AGN, Stern et al. IR-AGN, $f_{24\mu\text{m}}$ -selected) differ, we generally find that the IR-AGN samples have lower bias values than the X-ray AGNs or radio AGNs and therefore typically reside in lower mass dark matter halos ($\langle M_{\text{halo}} \rangle \sim 10^{11.5} h^{-1} \mathcal{M}_{\odot}$). We do not find a significant difference between the clustering amplitudes of samples identified using the Donley et al. IR-AGN or Assef et al. IR-AGN techniques. This is in agreement with Hickox et al. (2011), who consider somewhat higher redshift ($\langle z \rangle \sim 1.2$) and higher luminosity ($\langle L_X \rangle \sim 10^{44} \text{ erg s}^{-1}$) IR-AGNs than

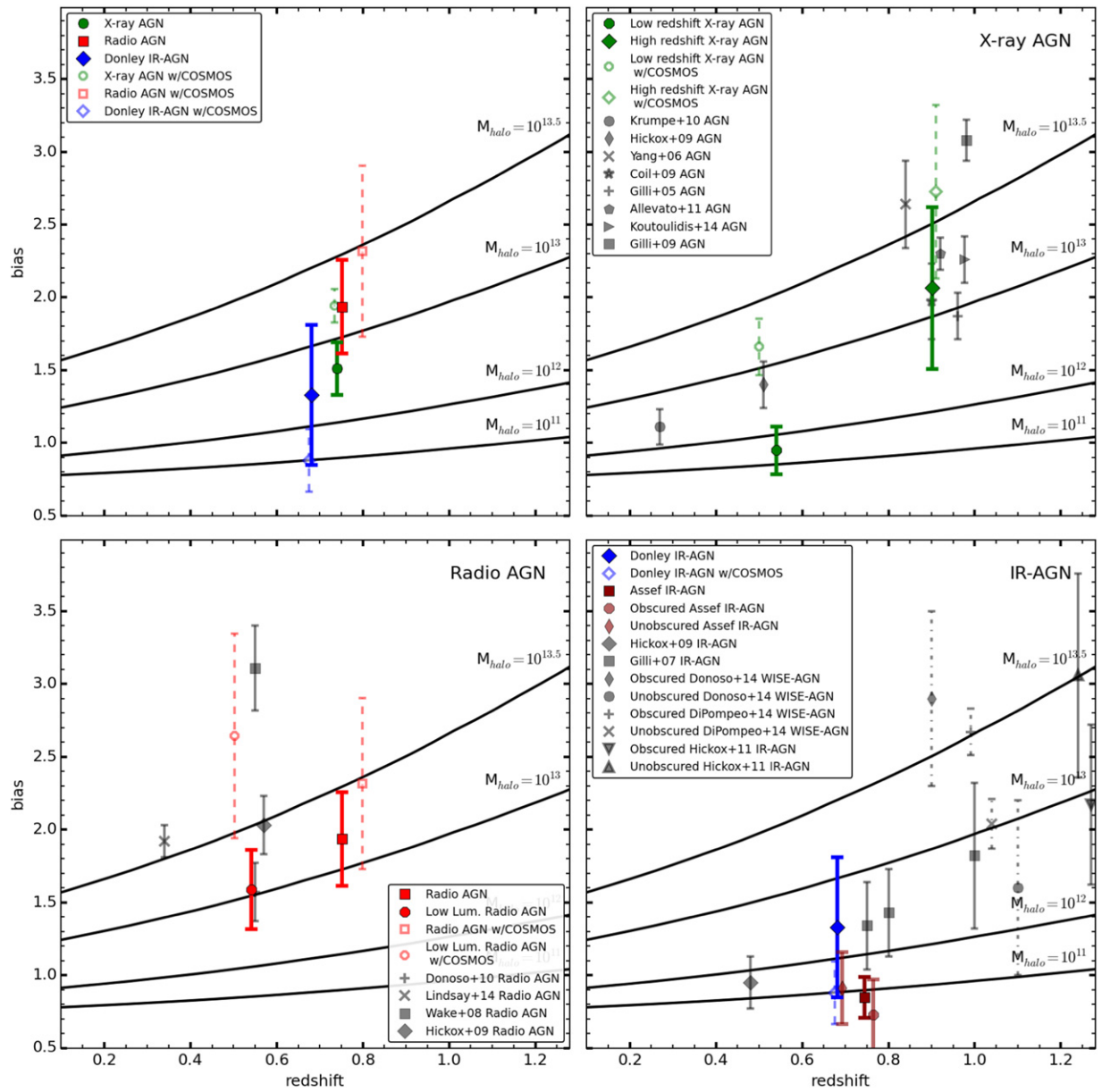


Figure 14. Comparison of the absolute bias as a function of redshift for AGNs identified at different wavelengths in the literature. Top left panel: bias of the X-ray AGNs (green circles), radio AGNs (red squares), and Donley et al. IR-AGNs (blue diamonds) presented in this paper, where the uncertainties are derived using jackknife resampling of the fields. In all panels, we show the estimated bias for samples in this paper. The filled symbols show the measured values excluding the COSMOS field. Black lines show constant dark matter halo mass ($M_{\text{halo}} = 10^{11} h^{-1} M_{\odot} - M_{\text{halo}} = 10^{13.5} h^{-1} M_{\odot}$). Top right panel: comparison of bias values in the literature for X-ray AGNs. Our results are shown in green, while gray points show results from the literature for $z \sim 1$. Bottom left panel: bias of the high-luminosity (red squares) and low-luminosity radio AGN samples (red circles). Gray points show results from the literature for radio AGNs. Bottom right panel: bias of the Donley et al. IR-AGN (blue diamond) and Assef et al. IR-AGN samples (red square). We show both the Assef et al. IR-AGN *WISE* obscured subsample (red thin diamond) and unobscured subsample (red thin circle). Gray points show results from the literature for IR-AGNs.

we do here. However, our results coupled with theirs suggest that there is not a significant difference in the clustering of obscured and unobscured IR-AGNs for a range of different redshifts and luminosities.

We also find no significant difference in the bias of the obscured and unobscured Assef et al. IR-AGNs. While there is a $\sim 29\%$ higher bias for the unobscured sources compared to the obscured sources, this is not significant ($\sim 1\sigma$). Our results do not agree with the angular clustering measurements from DiPompeo et al. (2014) or Donoso et al. (2014). Since we use spectroscopic redshifts, our results are more robust to differences in the redshift distributions of the two samples,

which could be driving the difference in the clustering amplitude of the obscured and unobscured samples in these other papers, as discussed above. Additionally, we find that the unobscured Assef et al. IR-AGNs have a brighter median W1 flux (~ 0.5 dex) than obscured Assef et al. IR-AGNs, which suggest that these samples have different effective luminosities, which will result in different redshift distributions. Since we require spectroscopic redshifts, our samples are smaller and therefore our statistical error bars are larger; however, the systematic errors associated with our spectroscopic samples should be much lower.

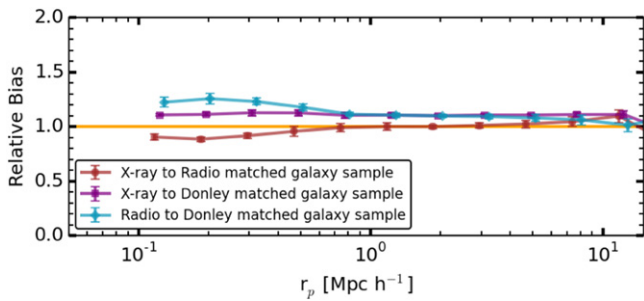


Figure 15. Relative bias for galaxy samples matched in stellar mass, sSFR, and redshift to AGN samples selected at different wavelengths. Error bars are from jackknife resampling of all fields. We show the scale-dependent relative bias for the X-ray-AGN- to radio-AGN-matched galaxies (dark red), X-ray-AGN- to Donley-et-al.-IR-AGN-matched galaxies (purple), and radio-AGN- to Donley-et-al.-IR-AGN-matched galaxies (cyan).

We note that the redshift success rate (the fraction of PRIMUS targets for which we derive a robust redshift) is very similar for the WISE IR-AGN sample ($\sim 72\%$) as for the full PRIMUS sample ($\sim 75\%$ Cool et al. 2013) when we account for the number of WISE IR-AGN sources outside the redshift range of PRIMUS, using the DiPompeo et al. (2014) WISE IR-AGN redshift distribution from the AGES survey (the AGN and Galaxy Evolution Survey Kochanek et al. 2012). We find a small trend (10% difference from the median) between the redshift success fraction and the observed W2 magnitude, where brighter WISE IR-AGNs have a higher redshift success fraction. We find a similar trend for both the obscured and unobscured sources, which would bias both samples to somewhat more luminous sources.

6.2. Does AGN Activity Depend on Halo Mass?

We show that differences in the host galaxy populations of AGNs identified at different wavelengths likely contribute to (if not fully account for) the differences in the inferred host dark matter halo masses of these AGNs. To account for the known host galaxy selection biases in AGN identification, we compare the clustering of each AGN sample to galaxy control samples with the same distribution of stellar mass, sSFR, and redshift in Section 5.6 and find no significant differences. Likewise, Leauthaud et al. (2015) find that X-ray AGNs do not reside in different halos than inactive galaxies, when they control for the stellar mass distribution of their detected X-ray AGNs. The lack of significant differences in the clustering amplitudes of AGNs and their galaxy control samples at even the $<2\sigma$ level strongly suggests that the physical mechanisms that are fueling and triggering AGNs either correlate with galaxy environment on scales much smaller than those that we probe here ($r_p \sim 0.1 h^{-1} \text{Mpc}$) or that AGN triggering is not correlated with the mass of the dark matter halo. For example, our results are consistent with Ellison et al. (2011), who use pairs of optically selected AGNs to identify a sharp increase in the activity of AGNs at close separations ($<80 h^{-1} \text{kpc}$); here we are sensitive to $>100 h^{-1} \text{kpc}$ only.

The validity of these statements relies on our ability to estimate the relevant galaxy properties and the fractional uncertainty in the clustering measurements. Both the stellar mass and sSFR estimates that we use improve upon previous techniques found in the literature, as we fit full stellar population synthesis models to the broadband SEDs of the AGN and galaxy samples in a consistent manner, to limit biases

that result from using individual bands or simple color-to-SFR correlations (e.g., Mostek et al. 2013). Additionally, we use relatively large samples of AGN and galaxy control samples with spectroscopic redshifts and maximize their measurement power by cross-correlating each with the PRIMUS and DEEP2 galaxy samples. This lowers the fractional uncertainty in our measurements and increases the significance of our results.

While we do not find a significant difference between the clustering of radio AGNs and matched galaxy control samples, Wake et al. (2008) and Donoso et al. (2010) find that radio AGNs are more clustered than their stellar mass-matched samples. Both compare mass-matched LRGs to radio AGNs at $z \sim 0.5$ and find that radio AGNs are significantly more clustered than the matched sample. While both authors examine radio AGNs with stellar masses and halo masses higher than those probed by our sample, neither of these papers explicitly control for differences in the sSFR distributions, which we find to be important in comparing different AGN samples to their host galaxies.

Finally, the matched galaxy control samples account for the individual selection biases from the AGN samples identified at different wavelengths. These biases depend on the depth of the sample and the different wavelengths that are used to identify the AGNs, both of which lead to differences in host galaxy properties (e.g., stellar mass, sSFR, and redshift). In Figure 15 we show the scale-dependent relative bias between matched galaxy control samples for our AGNs identified at different wavelengths. Similar to the relative biases found between the AGN samples, we find that the clustering strength of both the X-ray-AGN- and radio-AGN-matched galaxy control samples are higher than the Donley-et-al.-IR-AGN-matched galaxy control sample on all scales. The clustering strength of the radio-AGN-matched galaxy control sample is higher than the X-ray-AGN-matched galaxy control sample on small scales but is statistically similar on large scales.

The consistency between the matched galaxy control samples and the AGNs identified at different wavelengths can be used to better measure the clustering of AGNs. Differences in the host galaxy properties of AGNs selected at different wavelengths can be understood entirely as being due to selection effects (i.e., Mendez et al. 2013). We have shown here that these selection biases can entirely account for differences in the observed clustering properties of AGNs selected at different wavelengths. This confirms and extends the X-ray AGN results of Leauthaud et al. (2015) to AGNs detected in the radio and IR as well. The clustering of AGNs can therefore be understood in terms of the clustering of their host galaxy populations.

7. CONCLUSIONS

In this paper, we measure the clustering properties of X-ray, radio, and IR-selected AGNs in the PRIMUS and DEEP2 spectroscopic surveys. Within the X-ray AGN sample, we measure the dependence of clustering on X-ray luminosity, specific accretion rate, and hardness ratio. Within the radio AGN sample, we measure the dependence of clustering on radio luminosity, and within the IR-AGN sample, we measure the dependence of clustering on obscuration. As the AGNs in these samples span a wide range of specific accretion rates (which roughly traces Eddington ratio), we also investigate the dependence of clustering on specific accretion rate. We quantify the relative clustering strength (or relative bias)

between each AGN sample, as well as between the AGN samples and galaxy control samples that are matched in stellar mass, sSFR, and redshift. The main results from our work are as follows.

1. The clustering amplitude of observed X-ray AGNs, radio AGNs, and Donley et al. IR-AGNs at $0.2 < z < 1.2$ differ, indicating that they reside in different mass dark matter halos. X-ray AGNs and radio AGNs cluster similarly, and both are more clustered (at $\gtrsim 2\sigma$) than Donley et al. IR-AGNs, especially on scales $r_p < 1.0 h^{-1} \text{Mpc}$. We estimate that our X-ray AGN, radio AGN, and Donley et al. IR-AGN samples have median dark matter halo masses of $M_{\text{halo}} \sim 10^{12.9} h^{-1} M_{\odot}$, $M_{\text{halo}} \sim 10^{13.3} h^{-1} M_{\odot}$, and $M_{\text{halo}} \sim 10^{12.8} h^{-1} M_{\odot}$, respectively.
2. We find no significant dependencies ($< 2\sigma$) on the clustering amplitude with X-ray luminosity, specific accretion rate, or hardness ratio. We also find no significant difference in the clustering amplitude of radio-loud AGNs ($P_{1.4 \text{ GHz}} > 10^{24} \text{ Watts Hz}^{-1}$) compared to low-luminosity radio-detected AGNs ($P_{1.4 \text{ GHz}} < 10^{24} \text{ Watts Hz}^{-1}$).
3. There is no significant difference in the clustering of IR-AGN samples selected using either the Donley et al. (2012) or Assef et al. (2013) selection techniques. Using either selection, we find no significant difference in the clustering amplitude of obscured versus unobscured IR-AGNs, using *WISE*-optical colors to define obscuration. This suggests that previously published differences determined using angular clustering are dominated by differences and uncertainties in the redshift distributions of these sources.
4. The clustering amplitudes of the X-ray AGN, radio AGN and Donley et al. IR-AGN samples agree well with those of the matched galaxy control samples, which have the same distribution in stellar mass, sSFR, and redshift of the AGN host galaxy samples.

It is now understood that all AGN selection techniques have inherent biases no matter which waveband or technique is used. For example, AGNs identified using X-ray, radio, or MIR emission, as used here, are all more easily detected in massive host galaxies. This means that clustering results should always be interpreted as the clustering of *observed* AGN samples, above a given flux limit and therefore corresponding to a given stellar mass limit. It is clear that in addition to selection biases with stellar mass, there are additional biases with respect to the SFR of the host galaxy, where radio AGNs tend to be identified in quiescent galaxies and IR-AGNs have a bias toward being detected in star-forming host galaxies. This affects the observed clustering of the AGNs, which should only be interpreted relative to matched galaxy samples. The full population of AGNs among galaxies of all stellar masses is likely to exhibit different clustering properties than the observed AGNs, which are more easily identified in massive galaxies. When we match samples with respect to stellar mass, SFR, and redshift we find excellent agreement between the clustering of AGN host galaxies and inactive galaxies. Therefore, AGN clustering can be understood entirely in terms of galaxy clustering (and the dependence of clustering on galaxy properties) and AGN selection effects. Looking forward, theoretical models that include AGN evolution and predict the clustering of AGNs must include AGN selection biases in order to accurately

constrain the physical mechanisms triggering AGNs. Future observational results from surveys such as the Dark Energy Survey and the Hyper Suprime-Cam Survey will also need to account for these AGN selection effects as they push to lower AGN luminosities in order to tighten constraints on theoretical models.

We thank Andy Goulding for reducing the DEEP2 02 hr IRAC data and providing a source catalog.

Funding for PRIMUS has been provided by NSF grants AST-0607701, 0908246, 0908442, 0908354, and NASA grant 08-ADP08-0019. A.L.C. acknowledges support from NSF CAREER award AST-1055081. A.J.M. and J.A. acknowledge support from NASA grant NNX12AE23G through the Astrophysics Data Analysis Program. A.M.D. acknowledges support from The Grainger Foundation.

We thank the CFHTLS, COSMOS, DLS, and SWIRE teams for their public data releases and/or access to early releases. This paper includes data gathered with the 6.5 m *Magellan* Telescopes located at Las Campanas Observatory, Chile. We thank the support staff at LCO for their help during our observations, and we acknowledge the use of community access through NOAO observing time. We use data from the DEEP2 survey, which was supported by NSF AST grants AST00-71048, AST00-71198, AST05-07428, AST05-07483, AST08-07630, and AST08-08133. This study makes use of data from AEGIS Survey and in particular uses data from *GALEX*, Keck, and CFHT. The AEGIS Survey was supported in part by the NSF, NASA, and the STFC. Some of the data used for this project are from the CFHTLS public data release, which includes observations obtained with MegaPrime/MegaCam, a joint project of CFHT and CEA/DAPNIA, at the Canada–France–Hawaii Telescope (CFHT) which is operated by the National Research Council (NRC) of Canada, the Institut National des Science de l’Univers of the Centre National de la Recherche Scientifique (CNRS) of France, and the University of Hawaii. This work is based in part on data products produced at TERAPIX and the Canadian Astronomy Data Centre as part of the Canada–France–Hawaii Telescope Legacy Survey, a collaborative project of the NRC and CNRS. We also thank those who have built and operate the *Chandra* and *XMM-Newton* X-Ray Observatories. This research has made use of the NASA/IPAC Infrared Science Archive, which is operated by the Jet Propulsion Laboratory, California Institute of Technology, under contract with the National Aeronautics and Space Administration.

REFERENCES

- Aird, J., Alexander, D. M., Ballantyne, D. R., et al. 2015, *ApJ*, 815, 66
Aird, J., Coil, A. L., Moustakas, J., et al. 2012, *ApJ*, 746, 90
Allevato, V., Finoguenov, A., Cappelluti, N., et al. 2011, *ApJ*, 736, 99
Allevato, V., Finoguenov, A., Hasinger, G., et al. 2012, *ApJ*, 758, 47
Antonucci, R. R. J., & Ulvestad, J. S. 1985, *ApJ*, 294, 158
Appleton, P. N., Fadda, D. T., Marleau, F. R., et al. 2004, *ApJS*, 154, 147
Assef, R. J., Stern, D., Kochanek, C. S., et al. 2013, *ApJ*, 772, 26
Azadi, M., Aird, J., Coil, A., et al. 2015, *ApJ*, 806, 187
Barmby, P., Huang, J.-S., Ashby, M. L. N., et al. 2008, *ApJS*, 177, 431
Barro, G., Pérez-González, P. G., Gallego, J., et al. 2011, *ApJS*, 193, 13
Becker, R. H., White, R. L., & Helfand, D. J. 1994, in ASP Conf. Ser. 61, Astronomical Data Analysis Software and Systems III, ed. D. R. Crabtree, R. J. Hanisch, & J. Barnes (San Francisco, CA: ASP), 165
Becker, R. H., White, R. L., & Helfand, D. J. 1995, *ApJ*, 450, 559
Best, P. N., Kauffmann, G., Heckman, T. M., et al. 2005, *MNRAS*, 362, 25
Bigelow, B. C., & Dressler, A. M. 2003, *Proc. SPIE*, 4841, 1727
Blanton, M. R., & Roweis, S. 2007, *AJ*, 133, 734

- Booth, C. M., & Schaye, J. 2010, *MNRAS*, 405, L1
- Brusa, M., Civano, F., Comastri, A., et al. 2010, *ApJ*, 716, 348
- Brusa, M., Zamorani, G., Comastri, A., et al. 2007, *ApJS*, 172, 353
- Bruzual, G., & Charlot, S. 2003, *MNRAS*, 344, 1000
- Cappelluti, N., Ajello, M., Burlon, D., et al. 2010, *ApJL*, 716, L209
- Cappelluti, N., Brusa, M., Hasinger, G., et al. 2009, *A&A*, 497, 635
- Chabrier, G. 2003, *PASP*, 115, 763
- Charlot, S., & Fall, S. M. 2000, *ApJ*, 539, 718
- Chiappetti, L., Clerc, N., Pacaud, F., et al. 2013, *MNRAS*, 429, 1652
- Ciliegi, P., Zamorani, G., Hasinger, G., et al. 2003, *A&A*, 398, 901
- Civano, F., Elvis, M., Brusa, M., et al. 2012, *yCat*, 220, 10030
- Coil, A. L., Blanton, M. R., Burles, S. M., et al. 2011, *ApJ*, 741, 8
- Coil, A. L., Georgakakis, A., Newman, J. A., et al. 2009, *ApJ*, 701, 1484
- Coil, A. L., Newman, J. A., Croton, D., et al. 2008, *ApJ*, 672, 153
- Coil, A. L., Newman, J. A., Kaiser, N., et al. 2004, *ApJ*, 617, 765
- Condon, J. J. 1992, *ARA&A*, 30, 575
- Condon, J. J., Cotton, W. D., Greisen, E. W., et al. 1998, *AJ*, 115, 1693
- Cool, R. J., Moustakas, J., Blanton, M. R., et al. 2013, *ApJ*, 767, 118
- Cress, C. M., Helfand, D. J., Becker, R. H., Gregg, M. D., & White, R. L. 1996, *ApJ*, 473, 7
- Croton, D. J. 2009, *MNRAS*, 394, 1109
- Cutri, R. M., Wright, E. L., Conrow, T., et al. 2012, Explanatory Supplement to the WISE Preliminary Data Release Products, Tech. Rep. (IPAC/Caltech), 1
- Davis, M., Faber, S. M., Newman, J., et al. 2003, *Proc. SPIE*, 4834, 161
- Davis, M., & Peebles, P. J. E. 1983, *ApJ*, 267, 465
- de la Torre, S., Guzzo, L., Kovač, K., et al. 2010, *MNRAS*, 409, 867
- DiPompeo, M. A., Myers, A. D., Hickox, R. C., Geach, J. E., & Hainline, K. N. 2014, *MNRAS*, 442, 3443
- Donley, J. L., Koekemoer, A. M., Brusa, M., et al. 2012, *ApJ*, 748, 142
- Donley, J. L., Rieke, G. H., Rigby, J. R., & Pérez-González, P. G. 2005, *ApJ*, 634, 169
- Donoso, E., Li, C., Kauffmann, G., Best, P. N., & Heckman, T. M. 2010, *MNRAS*, 407, 1078
- Donoso, E., Yan, L., Stern, D., & Assef, R. J. 2014, *ApJ*, 789, 44
- Ellison, S. L., Patton, D. R., Mendel, J. T., & Scudder, J. M. 2011, *MNRAS*, 418, 2043
- Elvis, M., Civano, F., Vignali, C., et al. 2009, *ApJS*, 184, 158
- Faber, S. M., Phillips, A. C., Kibrick, R. I., et al. 2003, *Proc. SPIE*, 4841, 1657
- Fanaroff, B. L., & Riley, J. M. 1974, *MNRAS*, 167, 31
- Fanidakis, N., Georgakakis, A., Mountrichas, G., et al. 2013, *MNRAS*, 435, 679
- Ferrarese, L., & Ford, H. 2005, *SSRv*, 116, 523
- Franceschini, A., Hasinger, G., Miyaji, T., & Malquori, D. 1999, *MNRAS*, 310, L5
- Gebhardt, K., Bender, R., Bower, G., et al. 2000, *ApJL*, 539, L13
- Georgakakis, A., Nandra, K., Laird, E. S., Aird, J., & Trichas, M. 2008, *MNRAS*, 388, 1205
- Gilli, R., Daddi, E., Chary, R., et al. 2007, *A&A*, 475, 83
- Gilli, R., Daddi, E., Zamorani, G., et al. 2005, *A&A*, 430, 811
- Gilli, R., Zamorani, G., Miyaji, T., et al. 2009, *A&A*, 494, 33
- Goulding, A. D., Forman, W. R., Hickox, R. C., et al. 2012, *ApJS*, 202, 6
- Goulding, A. D., Forman, W. R., Hickox, R. C., et al. 2014, *ApJ*, 783, 40
- Hasinger, G. 2008, *A&A*, 490, 905
- Hickox, R. C., Jones, C., Forman, W. R., et al. 2009, *ApJ*, 696, 891
- Hickox, R. C., Myers, A. D., Brodwin, M., et al. 2011, *ApJ*, 731, 117
- Hopkins, P. F., & Hernquist, L. 2009, *ApJ*, 698, 1550
- Hopkins, P. F., Hernquist, L., Cox, T. J., et al. 2006, *ApJS*, 163, 1
- Hopkins, P. F., Hernquist, L., Cox, T. J., & Kereš, D. 2008, *ApJS*, 175, 356
- Hütsi, G., Gilfanov, M., & Sunyaev, R. 2014, *A&A*, 561, A58
- Iverson, R. J., Chapman, S. C., Faber, S. M., et al. 2007, *ApJL*, 660, L77
- Kauffmann, G., Heckman, T. M., White, S. D. M., et al. 2003, *MNRAS*, 341, 33
- Kochanek, C. S., Eisenstein, D. J., Cool, R. J., et al. 2012, *ApJS*, 200, 8
- Kormendy, J., & Ho, L. C. 2013, *ARA&A*, 51, 511
- Kormendy, J., & Richstone, D. 1995, *ARA&A*, 33, 581
- Koutoulidis, L., Plionis, M., Georgantopoulos, I., & Fanidakis, N. 2013, *MNRAS*, 428, 1382
- Kovač, K., Lilly, S. J., Cucciati, O., et al. 2010, *ApJ*, 708, 505
- Krumpe, M., Miyaji, T., & Coil, A. L. 2010, *ApJ*, 713, 558
- Laird, E. S., Nandra, K., Georgakakis, A., et al. 2009, *ApJS*, 180, 102
- Landy, S. D., & Szalay, A. S. 1993, *ApJ*, 412, 64
- Le Fèvre, O., Vettolani, G., Garilli, B., et al. 2005, *A&A*, 439, 845
- Leauthaud, A., J. Benson, A., Civano, F., et al. 2015, *MNRAS*, 446, 1874
- Lilly, S. J., Le Fèvre, O., Renzini, A., et al. 2007, *ApJS*, 172, 70
- Lonsdale, C. J., Smith, H. E., Rowan-Robinson, M., et al. 2003, *PASP*, 115, 897
- Lupton, R. 1993, *Statistics in Theory and Practice* (Princeton, NJ: Princeton Univ. Press)
- Madau, P., Ferguson, H. C., Dickinson, M. E., et al. 1996, *MNRAS*, 283, 1388
- Magliocchetti, M., Maddox, S. J., Hawkins, E., et al. 2004, *MNRAS*, 350, 1485
- Magorrian, J., Tremaine, S., Richstone, D., et al. 1998, *AJ*, 115, 2285
- Mandelbaum, R., Li, C., Kauffmann, G., & White, S. D. M. 2009, *MNRAS*, 393, 377
- Marconi, A., & Hunt, L. K. 2003, *ApJL*, 589, L21
- Mateos, S., Alonso-Herrero, A., Carrera, F. J., et al. 2012, *MNRAS*, 426, 3271
- Mateos, S., Alonso-Herrero, A., Carrera, F. J., et al. 2013, *MNRAS*, 434, 941
- Mathews, D. J., Newman, J. A., Coil, A. L., Cooper, M. C., & Gwyn, S. D. J. 2013, *ApJS*, 204, 21
- McBride, C. K., Connolly, A. J., Gardner, J. P., et al. 2011, *ApJ*, 726, 13
- McCracken, H. J., Peacock, J. A., Guzzo, L., et al. 2007, *ApJS*, 172, 314
- Mendez, A. J., Coil, A. L., Aird, J., et al. 2013, *ApJ*, 770, 40
- Meneux, B., Guzzo, L., de la Torre, S., et al. 2009, *A&A*, 505, 463
- Middleberg, E., Norris, R. P., Cornwell, T. J., et al. 2008, *AJ*, 135, 1276
- Mo, H. J., & White, S. D. M. 1996, *MNRAS*, 282, 347
- Mostek, N., Coil, A. L., Cooper, M., et al. 2013, *ApJ*, 767, 89
- Moustakas, J., Coil, A. L., Aird, J., et al. 2013, *ApJ*, 767, 50
- Mullaney, J. R., Alexander, D. M., Fine, S., et al. 2013, *MNRAS*, 433, 622
- Murphy, E. J., Condon, J. J., Schinnerer, E., et al. 2011, *ApJ*, 737, 67
- Newman, J. A., Cooper, M. C., Davis, M., et al. 2013, *ApJS*, 208, 5
- Norberg, P., Frenk, C. S., & Cole, S. 2008, *MNRAS*, 383, 646
- Norris, R. P., Afonso, J., Appleton, P. N., et al. 2006, *AJ*, 132, 2409
- Oliver, S., Rowan-Robinson, M., Alexander, D. M., et al. 2000, *MNRAS*, 316, 749
- Park, S. Q., Barmby, P., Fazio, G. G., et al. 2008, *ApJ*, 678, 744
- Peebles, P. J. E. 1980, *The Large-scale Structure of the Universe* (Princeton, NJ: Princeton Univ. Press)
- Pierre, M., Valtchanov, I., Altieri, B., et al. 2004, *JCAP*, 9, 11
- Puccetti, S., Fiore, F., D'Elia, V., et al. 2006, *A&A*, 457, 501
- Richstone, D., Ajhar, E. A., Bender, R., et al. 1998, *Natur*, 395, A14
- Salim, S., Rich, R. M., Charlot, S., et al. 2007, *ApJS*, 173, 267
- Schinnerer, E., Sargent, M. T., Bondi, M., et al. 2010, *ApJS*, 188, 384
- Schinnerer, E., Smolčić, V., Carilli, C. L., et al. 2007, *ApJS*, 172, 46
- Scoville, N., Aukel, H., Brusa, M., et al. 2007, *ApJS*, 172, 1
- Scranton, R., Johnston, D., Dodelson, S., et al. 2002, *ApJ*, 579, 48
- Serjeant, S., Negrello, M., Pearson, C., et al. 2010, *A&A*, 514, A10
- Sheth, R. K., Mo, H. J., & Tormen, G. 2001, *MNRAS*, 323, 1
- Sheth, R. K., & Tormen, G. 1999, *MNRAS*, 308, 119
- Sijacki, D., Springel, V., Di Matteo, T., & Hernquist, L. 2007, *MNRAS*, 380, 877
- Silk, J., & Rees, M. J. 1998, *A&A*, 331, L1
- Silverman, J. D., Kampeczyk, P., Jahnke, K., et al. 2011, *ApJ*, 743, 2
- Simpson, C., Martínez-Sansigre, A., Rawlings, S., et al. 2006, *MNRAS*, 372, 741
- Skibba, R. A., Smith, M. S. M., Coil, A. L., et al. 2014, *ApJ*, 784, 128
- Smith, R. E., Peacock, J. A., Jenkins, A., et al. 2003, *MNRAS*, 341, 1311
- Smolčić, V., Schinnerer, E., Scodreggio, M., et al. 2008, *ApJS*, 177, 14
- Soltan, A. 1982, *MNRAS*, 200, 115
- Springel, V., Di Matteo, T., & Hernquist, L. 2005, *ApJL*, 620, L79
- Stern, D., Assef, R. J., Benford, D. J., et al. 2012, *ApJ*, 753, 30
- Stern, D., Eisenhardt, P., Gorjian, V., et al. 2005, *ApJ*, 631, 163
- Sutherland, W., & Saunders, W. 1992, *MNRAS*, 259, 413
- Szokoly, G. P., Bergeron, J., Hasinger, G., et al. 2004, *ApJS*, 155, 271
- Tremaine, S., Gebhardt, K., Bender, R., et al. 2002, *ApJ*, 574, 740
- Ueda, Y., Akiyama, M., Ohta, K., & Miyaji, T. 2003, *ApJ*, 598, 886
- Ueda, Y., Watson, M. G., Stewart, I. M., et al. 2008, *ApJS*, 179, 124
- Urry, C. M., & Padovani, P. 1995, *PASP*, 107, 803
- van den Bosch, F. C. 2002, *MNRAS*, 331, 98
- Wake, D. A., Croom, S. M., Sadler, E. M., & Johnston, H. M. 2008, *MNRAS*, 391, 1674
- Willner, S. P., Ashby, M. L. N., Barmby, P., et al. 2012, *ApJ*, 756, 72
- Wright, E. L., Eisenhardt, P. R. M., Mainzer, A. K., et al. 2010, *AJ*, 140, 1868
- Yan, L., Donoso, E., Tsai, C.-W., et al. 2013, *AJ*, 145, 55
- Yang, Y., Mushotzky, R. F., Barger, A. J., & Cowie, L. L. 2006, *ApJ*, 645, 68
- Zehavi, I., Zheng, Z., Weinberg, D. H., et al. 2005, *ApJ*, 630, 1
- Zehavi, I., Zheng, Z., Weinberg, D. H., et al. 2011, *ApJ*, 736, 59
- Zheng, Z., Zehavi, I., Eisenstein, D. J., Weinberg, D. H., & Jing, Y. P. 2009, *ApJ*, 707, 554